LAWRENCE
LIVERMORE
NATIONAL
LABORATORY

LLNL-JRNL-413523

Hybrid Simulation of Laser-Plasma Interactions and Fast Electron Transport in Inhomogeneous Plasma

B. I. Cohen, A. Kemp, L. Divol

June 2, 2009

Journal of Computational Physics

Disclaimer

Simulation of Laser-Plasma Interactions and Fast Electron Transport in Inhomogeneous Plasma

B. I. Cohen, A. J. Kemp, and L. Divol

Lawrence Livermore National Laboratory, P. O. Box 808, Livermore CA 94551

Abstract

A new framework is introduced for kinetic simulation of laser-plasma interactions in an inhomogenous plasma motivated by the goal of performing integrated kinetic simulations of fast-ignition laser fusion. The algorithm addresses the propagation and absorption of an intense electromagnetic wave in an ionized plasma leading to the generation and transport of an energetic electron component. The energetic electrons propagate farther into the plasma to much higher densities where Coulomb collisions become important. The high-density plasma supports an energetic electron current, return currents, self-consistent electric fields associated with maintaining quasi-neutrality, and self-consistent magnetic fields due to the currents. Collisions of the electrons and ions are calculated accurately to track the energetic electrons and model their interactions with the background plasma. Up to a density well above critical density, where the laser electromagnetic field is evanescent, Maxwell's equations are solved with a conventional particle-based, finite-difference scheme. In the higher-density plasma, Maxwell's equations are solved using an Ohm's law neglecting the inertia of the background electrons with the option of omitting the displacement current in Ampere's law. Particle equations of motion with binary collisions are solved for all electrons and ions throughout the system using weighted particles to resolve the density gradient efficiently. The algorithm is analyzed and demonstrated in simulation examples. The simulation scheme introduced here achieves significantly improved efficiencies.

Key words:
PACS: 52.57.Kk, 52.65.Rr, 52.65.Pp

1. Introduction

The interaction of intense laser light with plasma leads to diverse phenomena of interest for applications such as laser fusion. The numerical simulation of laser-plasma interactions in multiple dimensions with the inclusion of kinetic effects is challenged by the large range of spatial and temporal scales [1, 2, 3] . The time step in particle-in-cell (PIC) simulation of plasmas using standard techniques must resolve the plasma oscillation everywhere, $\omega_{pe}\Delta t < O(1)$ for stability; the time step must resolve the laser frequency, $\omega_0\Delta t < O(1)$ for accuracy; the spatial mesh must resolve the electron Debye length, $\Delta x/\lambda_e < O(1)$ depending on the order of the spatial interpolation, [1] and the collisionless skin depth, $\Delta x\omega_{pe}/c < O(1)$, everywhere to control self-heating and ensure accuracy; and the Courant conditions on the speed of light and the particles must be resolved, $c\Delta t/\Delta x < 1$ [1].

In fast-ignition laser fusion [4] optical-wavelength laser light is incident on a plasma spanning a range of densities from vacuum to densities exceeding solid densities. If we consider plasma densities that are $10^3 - 10^4$ times the critical density n_c where the laser frequency ω_0 equals the local electron plasma frequency ω_{pe} and $n_c = 1.1 \times 10^{21}\mathrm{cm}^{-3}$ for a $1\,\mu$m laser wavelength, then the constraints on using standard particle simulation techniques solving Maxwell's equations and particle equations of motion using explicit time-integration methods are formidable. In consequence, many studies separate the simulation of fast ignition into fully electromagnetic studies of the laser-plasma interaction going from vacuum to densities somewhat higher than the critical density [5, 6, 7, 8] and then address the simulation of the transport of the fast electrons generated by the laser absorption occurring near the critical density to very high densities in a separate simulation using a reduction of Maxwell's equations [9, 10, 11, 12]. Here we introduce an algorithm that combines a conventional fully electromagnetic PIC simulation where the plasma is completely described in terms of particles and where the fields are solved with a reduced model in the high-density plasma. The composite algorithm marries the simulation of the laser-plasma interaction with the simulation of the electron transport, and thus seeks to be a more integrated simulation of fast ignition: the electron transport calculation is driven by the self-consistent absorption of the laser and the concomitant self-consistent generation of the fast electrons; the background plasma responds kinetically; and heat is transported self-consistently [9, 10, 11, 12].

Other approaches to the simulation of fast ignition in a plasma density

gradient have been exercised with varying degrees of success. In the work of Sentoku and Kemp [13], the plasma density is clamped in such a way as to limit the plasma frequency for purposes of accumulating charge densities and current densities to be used in solving Maxwell's equations, *i. e.* , an artificial upper bound is imposed on the plasma and current densities. However, the local electron and ion densities are allowed to climb to much higher values for purposes of computing collisions. The cutoff on the plasma density limits how large $\omega_{pe}\Delta t$ and how small the skin depth c/ω_{pe} become, which helps the simulation remain well behaved and relaxes the demands on computer resources. However, the calculated electric fields associated with the plasma currents are no longer consistent with the actual density influencing the collisions; and thus the resistive heating in the plasma is inconsistent in the region where the actual density exceeds the artificial cutoff. The algorithm that we present here has no artificial density cutoff and attempts to model the electromagnetic fields, collisions, and density gradients consistently.

Implicit particle simulation methods [3, 14, 15, 16, 17, 18, 19, 20, 21] underly a number of kinetic plasma simulation codes and are being used in studying fast ignition. [22] Implicit PIC permits the use of large values of $\omega_{pe}\Delta t$ subject to resolving wave and particle Courant conditions for sake of accuracy and controlling numerical heating and cooling [18, 23, 24] The implicit PIC algorithms alter the dielectric shielding in a plasma due to finite $\omega_{pe}^2\Delta t^2$. However, the numerical modification of the shielding is small if $\omega_{pe}^2\Delta t^2 << 1/k^2\lambda_e^2$ [24]. In the underdense region of the plasma, where $\omega_{pe} < \omega_0$, it is important to track the propagation and absorption of the laser accurately; and care should be taken in using an implicit PIC method so that it does not significantly damp the electromagnetic wave because of numerical dissipation [3, 18, 21].

Hybrid methods, wherein the plasma is composed of both fluid and particle species, have been used with success in many applications; and there is a mature literature [9, 10, 11, 12, 25, 26, 27, 28, 29]. The use of fluid equations to represent a major component of the plasma, such as, for example, the background electrons, while other components of the plasma are represented with a kinetic model, is well motivated if the kinetic features of the fluid species are ignorable, *e.g.*, if the fluid species is cold or so collisional as to be well approximated as a Maxwellian. The fluid representation introduces a computational efficiency by reducing the number of species requiring a kinetic description and/or by reducing the range of time and/or space scales. Important additional efficiencies may be accrued by introducing well-motivated analytical

reductions of the fluid equations for the fluid species, such as omitting inertial effects when the response of the fluid species can be approximated as adiabatic, collisional, or dominated by $\mathbf{E}\times\mathbf{B}$ drifts [10, 11, 12, 25, 26, 27, 28]. However, the fluid representation inevitably involves some closure approximation and loss of kinetic detail. Here we will exploit the use of reduced fluid equations to limit the kinds of high-frequency wave phenomena that can occur, but we will retain a kinetic description of all species. In some respects, a similar point of view is taken in the implicit-moment simulation methodology [15, 16, 22, 30].

In Figure 1 we illustrate the two-region nature of our algorithm. In the region of the plasma for electron densities $n_e \leq 100 n_c$, we solve the complete set of Maxwell's equations in finite-difference form [1, 31, 32] with relativisitic equations of motion for the plasma particles with binary collisions [13] for all of the electron and ion species throughout the domain. This description of the physics is valid if appropriate time steps, cell sizes, and statistical resolution are employed. At higher densities with a sufficiently cold background plasma, the plasma can become sufficiently collisional such that the plasma does not support high-frequency waves. The relatively cold background electrons are maintained close to a drifting Maxwellian and react to maintain quasineutrality (producing return currents to neutralize the energetic electron current driven by the laser absorption). There can be significant self-magnetic fields due to currents in the plasma. The cold, resistive electrons in the background plasma in the high-density region are well described by an Ohm's law with electron inertia neglected (Sec. II). The Ohm's law gives us a prescription for the self-consistent electric field related to the current in the resistive background plasma, while Ampere's law with the option of dropping or retaining the displacement current relates the sum of the background plasma and fast electron currents to the curl of the magnetic field. With explicit accumulations of the plasma ion and energetic electron currents from the particle data, Ampere's law gives us a prescription for the background electron current without having to accumulate the electron current on the grid in the high-density region. Faraday's law then relates the time derivative of the magnetic field to the curl of the electric field, which is used to update the magnetic field.

The resistive magneto-hydrodynamic (MHD) model proposed here for the background electron response in the high-density, collisional limit based on Ohm's law has been previously introduced and justified by several authors [10, 11, 12]. The reduced equations are shown to recover the results of

the solution of the complete Maxwell equations in an intermediate density region, $n_c << n_e \leq (50-100)n_c$ except that the reduced equations are less affected by particle noise. For even higher electron densities $n_e \gtrsim 50-100n_c$ the reduced equations are used exclusively. By dropping electron inertia in Ohm's law, the reduced equations in the high-density region are *not* subject to the restrictions that the plasma frequency, electron Debye length, and collisionless skin depth must be resolved. Numerical dissipation is easily controlled in both the low and high-density regions. An important physics element is that the resistivity in the Ohm's law should be self-consistent with the Coulomb collision operator influencing the particle motion; thus, a good quality collision operator is required [13]. An important distinction in our approach as compared to the model considered in the work of Davies, [10], Gremillet, *et al.*, [11], and Honrubia, *et al.* [12] in the high-density, collisional plasma region is that we retain a particle description for all of the electrons and ions in the plasma. The particle description for the background plasma in both the low and high-density plasma domains provides a natural distributed source for kinetic return currents throughout the system and a prescription for determining when a background electron should be promoted to a fast electron and vice versa, and the resistive heating of the background plasma is accommodated in a natural way in the presence of binary collisions using the collision operator introduced by Sentoku and Kemp [13]. A particle is called fast if its velocity exceeds $\alpha(T_e/m_e)^{1/2}$, where α is a free parameter (we find $\alpha = 5$ works well) and T_e is the local electron temperature. We will describe the model more completely in the next section.

In this study we restrict ourselves to a model for the plasma that assumes that the plasma parameter $n_e\lambda_e^3 >> 1$ where n_e is the electron number density and λ_e is the electron Debye length. Our representation of the collisional processes in the plasma, the use of a classical resistivity model, and our evaluation of terms in the electron momentum fluid equation for the background electrons depend on the assumption that the high-density region is a weakly coupled plasma. In fast-ignition scenarios the assumption that the plasma is weakly coupled can break down, *i.e.*, the plasma parameter is no longer large in some regions of the space-time domain. In such a circumstance both the collision model, the resistivity and other terms in Ohm's law must be modified to take into account the proper physics of the warm dense matter [10, 11, 12]. Such modifications can be made within the framework we introduce here, but we will defer this to future work; here we restrict our model to the case of a weakly coupled plasma with a classical Coulomb col-

lision model for sake of simplicity.

An outline for the rest of the paper is given as follows. In Sec. II the framework for the simulation model is introduced in detail, and equations are presented. An analysis of the properties of the algorithm is presented in Sec. III. Model simulations are also presented that address some of the numerical issues in the algorithm in a minimal rendering of the new framework. In Sec. IV one-dimensional and two-dimensional PIC simulations using the PSC code [31, 32] extended to incorporate the new framework for low and high-density plasma are presented. Comparisons are made between conventional, first-principles PIC simulation and simulations with the two-region model. Our two-region model allows the use of less spatial resolution at high densities where the electromagnetic skin depth becomes small and a larger time step because the certain numerical constraints are relaxed. This is illustrated in a one-dimensional example with an improvement in computational speed in excess of $40\times$. In two dimensions the improvement in computational speed realized in our example simulations is $> 500\times$. Our implementation of the two-region framework in the PSC code is a work in progress in some respects, and the research is ongoing. A summary and conclusions are presented in Sec. V.

2. Algorithm Equations

In conventional electromagnetic PIC simulation with explicit time integration, such as in the PSC code [31, 32], the electric and magnetic fields are laid down on a staggered grid; and the two curl equations in Maxwell's equations, Ampere's and Faraday's laws, are solved to advance the electric and magnetic fields, respectively:

$$\frac{\partial \mathbf{E}}{\partial t} = c\nabla \times \mathbf{B} - 4\pi \mathbf{J} \tag{1}$$

$$\frac{\partial \mathbf{B}}{\partial t} = -c\nabla \times \mathbf{E} \tag{2}$$

Some care is given to charge conservation in obtaining the current $\mathbf{J}$ [1, 32, 33, 34]. Charge conservation in the PSC code is described in Sec. 4. 5. 2 of Ref. [32]. In our model, relativistic particle equations for fast electrons, background electrons, and background ions with full Newton-Lorentz forces and a binary collision operator [13] are used throughout the system.

If the time step and the mesh spacing are chosen to resolve the plasma and light-wave frequencies, the Debye length, and skin depth throughout the domain and there is adequate statistical resolution, then a conventional simulation can track laser absorption and the transport of energetic electrons up to some modest plasma density. Use of higher-order spatial interpolation methods allows the mesh size to be larger than the electron Debye length without engendering excessive self-heating [1] at the expense of losing the ability to resolve scales of order or less than the electron Debye length, which are relevant to Debye sheaths and some wave dispersion effects. The PSC code uses linear area weighting for its interpolation scheme [1, 32].

In Fig. 2 is shown a conventional particle simulation in one dimension (1D) using PSC with binary collisions, 200 cells per micron, 100 ion particles per cell, and 400 electron particles per cell ($Z = 4$ for copper) in which 1 micron laser light is absorbed in a plasma density gradient with densities $\leq 360 n_c$. This simulation describes the interaction of a 40 fs fwhm Gaussian shaped laser pulse with a peak intensity of $5 \times 10^{19}\mathrm{W/cm}^2$ at a wavelength of 1 micron with a copper target at a (constant) ionization state $Z = 4$. The target features an exponential density gradient with a scale length of 1.5μm between electron densities $n_e << n_c$ and $4 \times 10^{23}\mathrm{cm}^{-3}$ followed by a density plateau of 15 microns length. To minimize the effect of numerical heating we used a resolution of 200 cells per micron and 100 particles per cell. The boundary conditions for particles and fields at the end of the box are 'absorbing' in the sense that particles are reflected at thermal velocities.

We note that for densities in excess of $n_e \sim 10 n_c$ in the one-dimensional simulation shown in Fig. 2 the electric field component E_z is well approximated by the resistive relation $E_z = \eta J_z^b$ allowing for the particle noise in the simulation that contributes to the electric field, where $\eta = m_e \nu_{ei}/n_e e^2$ is the classical resistivity [35], $\nu_{ei} = 0.51/\tau_{ei}$, $\tau_{ei}^{-1} = 4\sqrt{2\pi} ln\Lambda e^4 Z_i^2 n_i/(3\sqrt{m}_e T_e^{3/2})$ is the classical electron-ion collision frequency, and J_z^b is the sum of the background electron and ion currents. The $E_z = \eta J_z^b$ evaluation plotted in Fig. 2 is inferred for this simulation; PSC uses E_z determined by Maxwell's equations from first principles. The total J_z current is zero to very good approximation. Hence, $J_z^b \approx -J_z^f$ where J_z^f is the fast electron current. The agreement of the electric field with the resistive relation is not so surprising when we consider the equation describing momentum conservation for the relatively cold background electrons and recognize that the cold background

plasma is collisional:

$$n_e m_e(\frac{\partial}{\partial t} + \mathbf{v}_e \cdot \nabla)\mathbf{v}_e = -en_e\mathbf{E} - n_e m_e \nu_{ei}(\mathbf{v}_e - \mathbf{v}_i) \\ - en_e\mathbf{v}_e \times \mathbf{B}/c - \nabla p_e + (\frac{d}{dt})_{coll,e-f}\mathbf{P}_{mom,e} \quad (3)$$

where $\mathbf{v}_{e,i}$ are the fluid velocities for the background electrons and ions, $n_{e,i}$ is the background electron or ion density, p_e is the electron pressure (assumed a scalar here, but could be a tensor more generally), and the last term accounts for conservation of the collisional momentum being exchanged due to collisions of the fast electrons with the background electrons. The result observed in Fig. 2 suggests that the first two terms on the right side of Eq.(3) are the dominant terms in the high-density plasma, and balancing these two terms yields $\mathbf{E} = \eta(\mathbf{J}_e + \mathbf{J}_i)$, where $\mathbf{J}_{e,i}$ are the electron and ion contributions to the current from the background plasma exclusive of the fast-electron current. In writing Eq.(3) we tacitly assume that the plasma is weakly magnetized. The results at high density shown in Fig. 2 motivate the use of the reduced form of Eq.(3), *i.e.*, an Ohm's law. In general, the third term in Eq.(3), the $\mathbf{v}_e \times \mathbf{B}$ term, is included in two-dimensional simulations.

When there is a significant magnetic field present, the friction force of the ions on the electrons leads to a tensor resistivty $\boldsymbol{\eta}$,

$$\boldsymbol{\eta} = \eta_\parallel \hat{\mathbf{b}}\hat{\mathbf{b}} + \eta_\perp(\mathbf{I} - \hat{\mathbf{b}}\hat{\mathbf{b}}) - \eta_\wedge(\hat{\mathbf{b}}\times\ ) \quad (4)$$

A prescription for the tensor resistivity has been given in Sec. IV of Braginskii's review article, which includes the dependence of the resistivity tensor on the product of the electron cyclotron frequency and the characteristic electron-ion collision time, and on the charge state of the ions (see Eq.(4.30) and Table 2 in Braginskii [35]). In our simulations we have devised a simple interpolation formula to fit Table 2 in Braginskii's article, which gives the dependence of $\boldsymbol{\eta}$ on the ionic charge state:

$$\eta_\parallel = \frac{\alpha_0 m_e}{n_e e^2 \tau_{ei}} \quad \eta_\perp = (1 - \frac{\alpha_1' x^2 + \alpha_0'}{\Delta})\frac{m_e}{n_e e^2 \tau_{ei}} \quad \eta_\wedge = \frac{x(\alpha_1'' x^2 + \alpha_0'')}{\Delta})\frac{m_e}{n_e e^2 \tau_{ei}} \quad (5)$$

where

$$x = \Omega_e \tau_{ei} \quad \Omega_e = \frac{eB_0}{m_e c}$$
$$\tau_{ei} = \frac{3 m_e^{1/2} T_e^{3/2}}{4\sqrt{2\pi} \ln\Lambda e^4 Z^2 n_i}$$
$$\Delta = x^4 + \delta_1 x^2 + \delta_0 \quad \alpha_0 = 1 - \frac{\alpha_0'}{\delta_0}$$
$$\alpha_0' = Z^{-1.6}[1.837 + 0.0678(Z-1)^{1.6}],$$
$$\alpha_1' = Z^{-1}[6.416 + 4.63(Z-1)]$$
$$\alpha_0'' = Z^{-1.32}[0.7796 + 0.094(Z-1)^{1.32}]$$
$$\alpha_1'' = 1.704$$
$$\delta_0 = Z^{-1.8}[3.7703 + 0.0961(Z-1)^{1.8}]$$
$$\delta_1 = Z^{-1.05}[14.79 + 7.482(Z-1)^{1.05}],$$

Epperlein and Haines have calculated corrections to Braginskii's transport coefficients that are significant for $\Omega_e \tau_{ei} > 1$ [36]. The parameters in consideration for the fast-ignition simulations of interest to us satisfy $\Omega_e \tau_{ei} << 1$ in the high-density region in our model, and the corrections calculated by Epperlein and Haines are small (less than a few percent). Moreover, for these small magnetic fields ($\Omega_e \tau_{ei} << 1$), then $x << 1$ in the Braginskii tensor resistivity and the resistivity becomes a scalar, $\eta = \eta_\parallel$, which simplifies the Ohm's law. The magnetic field and plasma parameters used in the Braginski tensor resistivity are assumed to vary on time and space scales that are longer than the characteristic electron-ion collision time and the electron Larmor radius.

In fast ignition, when the electron transport in solid densities encounters higher and perhaps colder matter, the plasma parameter, $n_e \lambda_e^3$, may no longer be large. In this case the electron collisions are modified from classical Coulomb collisions in a weakly coupled plasma, which will alter the particle collision model and the self-consistent expression for the resistivity (derived from the electron-ion frictional force due to collisional drag) [10, 11, 12]. The framework introduced here should be able to accommodate these modifications, but we do not attempt this here.

We now assess the relative strengths of the various terms in Eq.(3) for parameters typical of fast-ignition calculations based on radiation-hydrodynamics simulations and experiments for conditions after the plasma has been com-

pressed but before fast electrons generated by the intense, short-pulse laser have heated the background high-density plasma: $T_e = T_i = 100\text{eV}$, $n_e \geq 10^2 n_c = 10^{23}\text{cm}^{-3}$, and scale length $l \sim 100\ \mu\text{m}$ in a hydrogen plasma. For these parameters $\lambda_e \sim 2 \times 10^{-8}\text{cm}$, $c/\omega_{pe} \sim 2 \times 10^{-6}\text{cm}$, $\omega_{pe} \sim 2 \times 10^{16}\text{s}^{-1}$, $\omega_0 \sim 2 \times 10^{15}\text{s}^{-1}$, a characteristic ion acoustic frequency $(\lambda_e/l)\omega_{pi} \sim 10^{12}\text{s}^{-1}$, and characteristic collision frequencies $\nu_e \sim 5 \times 10^{15}\text{s}^{-1}$ and $\nu_i \sim 8 \times 10^{13}\text{s}^{-1}$. The parameters chosen are somewhat arbitrary, but are intended to be representative. At this density the electron plasma and ion acoustic waves are significantly damped by collisions. As the plasma density increases, the electron plasma frequency increases proportional to $\sqrt{n_e}$; the acoustic frequency is approximately invariant if T_e is relatively constant; and the collision frequencies increase approximately linearly in n_e. Thus, the collisional damping of the longitudinal waves is more pronounced as the density increases. Before comparing the terms in Eq.(3), we divide both sides by $(n_e m_e)$. We assume that the high-density plasma background evolves on the transport time scale as dictated by the collision processes. The axial motion of the background electrons provides a return current to neutralize the fast electrons. An upper limit on the fast-electron current is set by arguing that the velocity of the fast electrons cannot exceed c, the speed of light; and its density cannot much exceed the density of all of the electrons near the critical density, n_c. Then at the higher densities the background plasma's return current is bounded in magnitude very approximately by $en_c c$, and the drift velocity of the background electrons is then limited in magnitude to $(n_c/n_e)c$. The inertia terms on the left side are then $(\partial/\partial t + \mathbf{v_e} \cdot \nabla)\mathbf{v_e} \rightarrow (O(\omega) + O(\mathbf{v_e}/l))\mathbf{v_e}$, where $v_e < (n_c/n_e)c$, $\omega < \omega_0 \sim 2 \times 10^{15}\text{s}^{-1}$, and $v_e/l < (n_c/n_e)c/l \sim (n_c/n_e)$ $3 \times 10^{12}\text{s}^{-1}$. The electric field term is assumed to balance the electron-ion drag term (leading directly to $\boldsymbol{\eta} \cdot \mathbf{J}$), which is of order $\nu_e v_e \sim 5 \times 10^{15}\text{s}^{-1}\text{v}_\text{e}$. The Lorentz force term on the right side of the Ohm's law is of order $\Omega_e v_e \leq \omega_0 v_e \sim 2 \times 10^{15}\text{s}^{-1}\text{v}_\text{e}$ if a signficant magnetic field arises with electron cyclotron frequency of order the laser frequency as is observed in simulations [12]. This term is smaller than the drag term but is non-negligible. The magnitude of the pressure term can be estimated as $(T_e/m_e)/l \sim 2 \times 10^{-4}$ $c^2/l \sim 6 \times 10^8\text{s}^{-1}\text{c}$ and is relatively small unless a steep gradient should form. The collisions of the fast electrons on the background electrons lead to the last term on the right side of Eq.(3) which is small in $(n_f/n_e)(\gamma_f c/v_e)(\nu_f/\nu_e)$ where n_f is the density of fast electrons $n_f \leq n_c$, γ_f is the relativistic factor for the fast electrons, and ν_f is the characteristic collision frequency of the fast electrons, $\nu_f << \nu_e$. We will also omit this momentum exchange term

in the simulation examples.

For fast-ignition simulation in high-density collisional plasmas we drop the inertia terms on the left side of the Eq.(3) and recast the resulting Ohm's law in the following form for the background plasma:

$$\mathbf{E} = \boldsymbol{\eta} \cdot (\mathbf{J}_e + \mathbf{J}_i) - \mathbf{v_e} \times \mathbf{B}/c \\ - \nabla p_e/(en_e) + (\frac{d}{dt})_{coll,e-f} \mathbf{P}_{mom,e}/(en_e) \tag{6}$$

This equation will yield an explicit, algebraic determination of the electric field. We are using a scalar pressure $p_e = n_e T_e$ in the Ohm's law in our high-density hybrid model, which can be generalized to a tensor pressure with no difficulty.

In keeping with the reduction of the Ohm's law based on the dominance of collisional effects in the high-density region of the plasma ($n_e >> n_c$), we drop the displacement current in Ampere's law, Eq.(1), and recast that equation to solve for the sum of the electron and ion currents in the background plasma exclusive of the fast-electron current $\mathbf{J_f}$, $\mathbf{J}_e + \mathbf{J}_i = \mathbf{J} - \mathbf{J}_f$,

$$\mathbf{J}_e + \mathbf{J}_i = \frac{c}{4\pi} \nabla \times \mathbf{B} - \mathbf{J}_f \tag{7}$$

$\mathbf{J}_f$ is the current from the fast electrons (those with speeds $> \alpha(T_e/m_e)^{1/2}$). The sum of the electron and ion currents in the background plasma is used in Eq.(6), which determines $\mathbf{E}$ in the high-density region. Charge conservation and the relation between the charge density and the current accumulations for the fast electrons and the ions are handled in the high-density region exactly as in the low-density region [32] . However, in the high-density region Eq.(7) is used to solve for $\mathbf{J}_e$; and $\mathbf{J}_e$ is not accumulated on the grid except as a diagnostic.

In the absence of the displacement current in Ampere's law, we can take the divergence of Eq.(7) to arrive at $\nabla \cdot (\mathbf{J}_e + \mathbf{J}_i + \mathbf{J}_f) = 0$. Use of the continuity equations then leads to the constraint on charge neutrality from which we calculate the electron charge density:

$$n_e = Z n_i - n_f \tag{8}$$

where n_i and n_f are the ion and fast-electron charge densities accumulated directly from the particles on the grid. Use of n_e from Eq.(8) in Ohm's law binds the electron density and the electron dynamics to the overall charge

neutrality constraint in the high-density plasma. This deduced charge density should be a good approximation to the charge density from the background electrons accumulated on the grid. Equation (8) is one prescription for determining n_e in Ohm's law. Alternatively we can use the n_e determined directly from the particle electrons with and without a correction to the background electron particle drift so that the total current is consistent with Ampere's law in the high-density region in each cell. It is these latter two options that we employ in the PSC PIC-hybrid simulations. Note that the divergence of Ampere's law plus the continuity equation implies Poisson's equation (and quasi-neutrality if the divergence of the displacement current is small). Because we are dividing by the electron density n_e in certain terms on the right side of the Ohm's law and computing the gradient of the scalar electron pressure $n_e T_e$, we find that temporally or spatially smoothing n_e is needed to deal with particle noise. In doing time averages we use a simple lag average over a few laser cycles, $< n_e >^n = \alpha n_e^n + (1-\alpha) < n_e >^{n-1}$ where $1/\alpha$ is the memory in time steps of the lag average. We will compare the grid-interpolated particle electron current in the full PIC and two-region hybrid simulations in Sec. 4.

The remaining terms on the right side of Eq.(6) are determined as follows. The background electron mean drift can be determined in either of two ways. A direct calculation can be made from the first moment of the particle electrons accumulated locally on the spatial grid, which has to be computed as part of calculating the local electron temperature from the background electrons. An alternative means is to subtract the fast-electron and ion currents explicitly accumulated from the particles from the sum of the electron and ion currents to obtain the electron current $\mathbf{J}_e$, from which $\mathbf{v}_e = -\mathbf{J}_e/(en_e)$. The background electron temperature is computed from the time-dependent second velocity moment of the background particle electrons deposited on the spatial grid. The second velocity moment can be noisy and require spatial and/or temporal smoothing. There is significant relevant experience with the pressure term reported in the literature on the implicit moment method [15, 16, 30]. The resistivity coefficient in the Ohm's law depends explicitly on the background electron temperature, which is determined from the particle representation of the background electrons and evolves as the electrons cool or heat. The term associated with the collisional momentum exchange of the background electrons with the fast electrons in Eq.(6) could be computed directly from the particle collisions between the fast and background electrons.

The prescription given here for the evaluation of the electric field from Ohm's law using moments of the particle velocity distributions emulates some of the philosophy of the implicit moment equations method, while incorporating some physics-based simplifications of the Ohm's law appropriate for studying the macroscopic-timescale transport of the fast electrons in the high-density collisional plasma. The simplifications used in the Ohm's law, *i.e.*, omitting the electron inertia terms and in some cases retaining only the first two or three terms on the right side of Eq.(6), as motivated by consideration of the physical parameters encountered in the collisional high-density fast-ignition plasmas, share a common basis with earlier work using hybrid algorithms [10, 11, 12, 25, 26, 27, 28].

From the curl of **E** in Eq.(2) the magnetic field is updated throughout the low and high-density regions. With **E** and **B** determined, the particle equations of motion are advanced for the trajectories of the fast electrons and the background plasma electrons and ions throughout the plasma. The fast electrons are differentiated from the assumed near-Maxwellian background electrons by having been heated by the laser when the laser is absorbed near the critical density. The contribution to the total current from the fast electrons is computed at every time step. To differentiate the fast electrons from the colder background electrons in the low-density region, when an electron achieves a speed exceeding $5\sqrt{T_e/m_e}$ in the background plasma, where the background scalar electron temperature T_e is computed locally from the background particle electrons at the previous time step, the electron is declared to be a fast electron until its speed drops below this threshold. Note that the threshold speed is allowed to evolve with the scalar electron temperature $T_e(\mathbf{x}, t)$. The choice of $5\sqrt{T_e/m_e}$ for a cutoff is sufficient to capture the lowest moments of the background electron velocity distribution up through the heat flux to high degree of accuracy. We can calculate the density, mean drift, scalar pressure, and scalar temperature moments of the background particle electrons to evaluate quantities on the right side of the Ohm's law, Eq.(6), as needed.

With relatively little additional effort the displacement current can be restored in Eq.(7) and a reasonably straightforward solution for the electric field can be obtained:

$$\mathbf{J}_e^n + \mathbf{J}_i^n = (c/4\pi)\nabla \times \mathbf{B}^n - \mathbf{J}_f^n - (\mathbf{E}^{n+1/2} - \mathbf{E}^{n-1/2})/4\pi\Delta t \tag{9}$$

$$\begin{aligned}\mathbf{E}^* = \eta(\mathbf{J}_e^n + \mathbf{J}_i^n) \\ - (en_e^n)^{-1}\nabla p_e^n - \mathbf{v}_e^n \times \mathbf{B}^n/c\end{aligned} \tag{10}$$

$$\mathbf{E}^{n+1/2} = [2\mathbf{E}^* - (1-\epsilon_1)\mathbf{E}^{n-1/2}]/(1+\epsilon_1) \tag{11}$$

Equations (9) and (11) are used in Eq.(10) to determine $\mathbf{E}^*$. These equations are linear in $\mathbf{E}^{n+1/2}$ and merely require an algebraic solution. By including the displacement current, we include charge separation effects. In place of Eq.(8), taking the divergence of Ampere's law including the displacement current and using the continuity equation lead to the following form of Poisson's equation to determine the background electron charge density in the high-density region:

$$n_e^n = Zn_i^n - n_f^n - \nabla \cdot \mathbf{E}^\dagger/4\pi e \tag{12}$$

For simplicity in solving the Ohm's law for the electric field, we suggest that the calculation of n_e from Eq.(12) use an explicit electric field $\mathbf{E}^\dagger = \mathbf{E}^{n-1/2}$ in the computation of the $-\nabla\cdot\mathbf{E}^\dagger/4\pi e$ term. The analysis and examples presented in the following sections of this paper only address the algorithm based on Eqs.(2-7) except where noted. With the displacement current included as described, analysis indicates that the important stability constraints and all of the accuracy constraints associated with the explicit solution of the high-density model equations excluding the displacement current persist.

In the implementation of our two-region model, we advance the particle equations of motion with binary collisions throughout the domain. In the low-density region and over a few cells (controlled as an input parameter) beyond the interface between the regions, Ampere's law is solved in conventional explicit fashion to update the electric field. On the high-density side and over a few cells on the low-density side of the interface between regions (also controlled as an input parameter), Ampere's and Ohm's laws are solved simultaneously for the electric field. The solution for the electric field is algebraic and requires no internal boundary condition at the interface between regions. In the region near the interface where two alternative expressions for the electric field are available, we have the following options: spatially interpolate between the two solutions, spatially smooth the electric field in the region around the interface, or use the low(high)-density solution on the

low(high)-density side with no interpolation or spatial smoothing. Faraday's law is solved throughout the domain to update the magnetic field from the curl of the electric field. Conventional boundary conditions on the electromagnetic fields and the particle motion at the system boundaries are used.

Energy conservation and flow in the high-density region differ from that in the low-density region as follows. The continuum equations in the low-density region yield the standard relations:

$$\frac{\partial}{\partial t}\left(\frac{E^2}{8\pi}+\frac{B^2}{8\pi}\right) = -\mathbf{E}\cdot\mathbf{J} - c\nabla\cdot\frac{\mathbf{E}\times\mathbf{B}}{4\pi} \tag{13}$$

where $\mathbf{J} = \sum_s \mathbf{J}_s$ and the sum is over all species s computed locally in space; and in the absence of explicit sources and sinks of plasma kinetic energy, the time derivative of the (relativistic or non-relativistic) kinetic energy density KE_s for each species satisfies

$$\frac{d}{dt}KE_s = \mathbf{E}\cdot\mathbf{J}_s \tag{14}$$

where s designates the species.

The continuum equations in the high-density region (omitting the displacement current) yield

$$\frac{\partial}{\partial t}\left(\frac{B^2}{8\pi}\right) = -\mathbf{E}\cdot\mathbf{J} - c\nabla\cdot\frac{\mathbf{E}\times\mathbf{B}}{4\pi} \tag{15}$$

where $\mathbf{J} = \mathbf{J}_i + \mathbf{J}_e + \mathbf{J}_f$. We can then use Eq.(6) to evaluate $\mathbf{E}$. In the limit that the resistivity dominates the right side of Eq.(6), we obtain the following relation:

$$\frac{\partial}{\partial t}\left(\frac{B^2}{8\pi}\right) = -\mathbf{J}\cdot\boldsymbol{\eta}\cdot(\mathbf{J}_e+\mathbf{J}_i) - c\nabla\cdot\frac{\mathbf{E}\times\mathbf{B}}{4\pi} \tag{16}$$

and Ampere's law is used to evaluate $\mathbf{J}$, *viz.*, $\mathbf{J} = c\nabla\times\mathbf{B}/4\pi$. However, Eq.(14) still dictates the relation between the Joule heating $\mathbf{E}\cdot\mathbf{J}_s$ involving the *particle* currents and the time derivative of the kinetic energy densities of each species. In the high-density region with the displacement current omitted, the field energy is composed only of the magnetic energy, which is dissipated in part by resistive heating of the background plasma if there is a net current and can be driven up or down by the net electromagnetic flux through the boundaries of the domain.

In the high-density plasma the reduced field equations support neither light waves nor electron plasma waves because of the high collisionality, the neglect of electron inertia in the Ohm's law, and the omission of the displacement current in Ampere's if this option is used. The reduced Maxwell's equations can be described as the Darwin, quasi-neutral limit of Maxwell's equations when the displacement current is omitted. The reduced equations support self-consistent magnetic and electric fields arising from the currents in the plasma, charge polarization, and kinetic return currents to maintain quasi-neutrality for long wavelength and low-frequency phenomena. The electric and magnetic fields are assumed continuous across the boundary between regions, which requires that the Ohm's law and the neglect of the displacement current be good approximations near the boundary between the two regions. The particle equations of motion for the fast electrons and the background plasma are integrated across the entire domain without regard for the boundary between the two regions. Thus, the particle fluxes and currents throughout the plasma are reasonably continuous, and the resistive heating of the background plasma is modeled with a kinetic description. Coulomb collisions [13] of the charged particles are modeled throughout with sufficient accuracy so that there is consistency with the resistivity in the Ohm's law. Figure 2 illustrates that this is possible.

By using a reduced physics model in the high-density, collisional plasma, we intentionally abdicate the ability to simulate all of the physics that is supported by a more complete set of equations. For example, electron plasma oscillations and light waves are not admitted by the equations used in the high-density region. In consequence, electron two-stream and electron beam-plasma instabilities cannot occur in the high-density plasma. However, owing to the high collisionality (the electron-electron and electron-ion collision frequencies are substantial fractions of the electron plasma frequency) the high-density plasma is stable with respect to these instabilities. In contrast, an instability like the ion-acoustic drift instability could occur in our high-density model equations if the relative drift of warm electrons with respect to the ions exceeds the ion sound speed and if ion-ion collisions and gradients that affect the instability are not too strong. Furthermore, our equations also allow low-frequency Weibel-like and current filamentation instabilities to occur in both the low and high-density regions.

3. Analysis of the algorithm

To understand what numerical constraints apply to the reduced equations in the high-density region, we introduce a model set of finite-difference equations and analyze some of the properties of these difference equations in this section. The model finite-difference equations capture the main elements of the high-density equations. We also present some results from the numerical solution of the model finite-difference equations. The analyses provide insight into the numerical properties of the algorithm: numerical stability, dispersion, and accuracy. Here we focus just on the time-integration issues and introduce difference equations in time.

$$\mathbf{J}_e^n + \mathbf{J}_i^n = (c/4\pi)\nabla \times \mathbf{B}^n - \mathbf{J}_f^n \tag{17}$$

$$\begin{aligned}\mathbf{E}^* = \eta(\mathbf{J}_e^n + \mathbf{J}_i^n) \\ - (en_e^n)^{-1}\nabla n_e^n T_e^n + (en_e^n)^{-1}\mathbf{J}_e^n \times \mathbf{B}^n/c\end{aligned} \tag{18}$$

$$\mathbf{E}^{n+1/2} = [2\mathbf{E}^* - (1-\epsilon_1)\mathbf{E}^{n-1/2}]/(1+\epsilon_1) \tag{19}$$

$$\frac{\mathbf{B^{n+1}} - \mathbf{B^n}}{\Delta t} = -c\nabla \times \mathbf{E^{n+1/2}},\ \mathbf{B^{n+1}} = ... \tag{20}$$

$$\mathbf{B}^{n+1/2} = (\mathbf{B}^{n+1} + \mathbf{B}^n)/2 \tag{21}$$

$$\mathbf{x}^{n+1/2} = \mathbf{x}^n + \frac{\Delta t}{2}(1-\epsilon_2)\mathbf{v}^n \tag{22}$$

$$\begin{aligned}\mathbf{v}^{n+1} = \mathbf{v}^n + \frac{q\Delta t}{m}[\mathbf{E}^{n+1/2} \\ + (\mathbf{v}^{n+1} + \mathbf{v}^n) \times \mathbf{B}^{n+1/2}/c] - \nu\Delta t\mathbf{v}^n\end{aligned} \tag{23}$$

$$\mathbf{x}^{n+1} = \mathbf{x}^n + \frac{\Delta t}{2}(1+\epsilon_2)\mathbf{v}^{n+1} \tag{24}$$

where $\epsilon_{1,2}$ are centering parameters and $\{\mathbf{x}, \mathbf{v}\}$ are the particle positions and velocities. In Eq.(18) we have omitted the term deriving from momentum exchange between the fast electrons and the background electrons; it is straightforward to include this term. The currents $\mathbf{J}_i^n$ and $\mathbf{J}_f^n$ are accumulated on the grid using particle data $\{\mathbf{x}, \mathbf{v}\}^n$. As written, the finite-difference equations, Eqs.(17-24), describe an explicit integration scheme with the displacement current term and the electron inertia term in Ohm's law omitted.

In the electrostatic limit with no background magnetic field and no fast electrons, the high-density equations admit ion acoustic waves. From Eq.(17),

$\mathbf{J}_e + \mathbf{J}_i = 0$, and we set $n_e = Zn_i$ in Eq.(18). Using standard techniques for the analysis of the normal modes of the finite-difference equations,[1, 3, 18] we linearize the difference equations, take $Z = 1$, define $\lambda \equiv E_z^{n+1}/E_z^n = \exp(-i\omega\Delta t)$ for a monochromatic wave, and obtain the following dispersion relation from the determinant of the coefficients of the system of linear equations:

$$[\lambda(1+\epsilon_1) + (1-\epsilon_1)]\frac{(\lambda-1)(\lambda-1+\nu_{ii}\Delta t)}{4\lambda} = \\ -\frac{k^2c_s^2\Delta t^2}{4}[\lambda(1+\epsilon_2) + (1-\epsilon_2)] \tag{25}$$

where ν_{ii} is the ion-ion collision frequency, $c_s^2 = T_e/m_i$ is the square of the sound speed, T_e is the electron temperature, and the electrons are assumed to respond adiabatically. For $\epsilon_1 = \epsilon_2$ there are two branches of the dispersion relation:

$$\lambda = -(1-\epsilon_1)/(1+\epsilon_1) \tag{26}$$

$$\frac{(\lambda-1)(\lambda-1+\nu_{ii}\Delta t)}{4\lambda} = -\frac{k^2c_s^2\Delta t^2}{4}$$

$$\rightarrow \sin(\omega\Delta t/2) \approx \pm(kc_s\Delta t/2)(1 \mp i\nu_{ii}\Delta t/2) \tag{27}$$

The mode described by Eq.(26) is a marginally stable odd-even oscillation for $\epsilon_1 = 0$ and is damped for $\epsilon_1 > 0$. Alternatively, with $\epsilon_1 = 0$, occasional averaging, $\mathbf{E}^{n+1/2} = (\mathbf{E}^{n+1/2} + \mathbf{E}^{n-1/2})/2$ will remove the odd-even mode. The mode corresponding to Eq.(27) is the ion acoustic wave with damping due to ion-ion collisions. With $\epsilon_1 \neq \epsilon_2$ the ion acoustic wave can be destabilized for small values of ν_{ii}. By relating n_e for use in Ohm's law to Zn_i and the ion dynamics through the use of Eq.(8) (or Eq.(12)), then the ion dynamics and the adiabatic response of the electrons are properly married to charge neutrality (or Poisson's equation) to obtain the self-consistent determination of the ion acoustic wave. If instead n_e is determined by the electron particle equations and used in the Ohm's law with no charge neutrality constraint and Ampere's law is used to close the system, then a somewhat redundant description of the electrons is introduced, the coupling of the ion dynamics back into the electric field solution is lost, and there is no ion acoustic wave. If the displacement current is retained as in Eq.(9) and n_e is determined by Eq.(12), then we recover the standard dispersion relation for ion acoustic waves including the dispersive correction due to charge separation effects: $\omega^2 = k^2c_s^2/(1 + k^2\lambda_e^2)$ in the limit that $\nu_{ii} = 0$ and $\Delta t = 0$.

We have integrated the model difference equations, Eqs.(17 -24), in the electrostatic limit with a small-amplitude random noise source added to the right side of Eq.(18) and with the prescriptions that the perturbed electron density is given by $\delta n_e = -\nabla n_0 x_e$ and the electron and ion displacements and velocities are fluid-like quantities shared by all electrons and ions in a cell. We introduce the quantity N_f which represents the number of time steps between the occasional averaging of the electric field at successive time steps. Figure 3 shows the results of integrations of the model difference equations in the electrostatic limit for ion acoustic waves with a finite noise source, no collisions, $\epsilon_1 = \epsilon_2 = 0$ or 0.02, $e/m = 1$, $kc_s = 1$, $N_f = \infty$ or 75, velocity amplitude perturbation $\delta v = 10^{-4}$, and 10% random noise amplitude relative to the wave amplitude. The spatial dependence has been Fourier analyzed, and only a single wavenumber k is retained. For $kc_s\Delta t = 0.1$ the fluid velocity at a given position vs. time oscillates at the acoustic frequency. With no decentering and no periodic averaging there is an excursion in the electric field energy, but no numerical instability. With decentering or periodic averaging, the solutions are well behaved.

If a small amount of decentering is introduced in the equations of motion in the finite-difference equations to control the odd-even mode, what might this decentering do to solutions of the difference equations in the low-density region where the electron plasma oscillation is an additional electrostatic normal mode? We replace Eqs.(17-24) in the electrostatic limit ($\mathbf{B} = 0$) with

$$\frac{\mathbf{E}^{n+1/2} - \mathbf{E}^{n-1/2}}{\Delta t} = -4\pi(\mathbf{J}_e^n + \mathbf{J}_i^n), \tag{28}$$

solve for $\mathbf{E}^{n+1/2}$, add a small noise source, and use Eqs.(22 - 24) for the cold-plasma, fluid-like response to the electric field. These equations support electron plasma oscillations. Figure 4 displays the results of integrating these equations with $\omega_{pe}\Delta t = 0.1$, $e/m = 1$, $\omega_{pe} = 1$, no periodic time-averaging of successive time levels, no collisions, displacement amplitude perturbation $\delta x = 10^{-4}$, and 10% random noise amplitude relative to the wave amplitude, for $\epsilon_2 = 0$ and 0.02. The fluid displacement oscillates at the electron plasma frequency. The decentering contributes a small amount of damping scaling with $\epsilon_2\omega_{pe}\Delta t$. In the absence of physical dissipation there is no fluctuation-dissipation theorem [1] for the model system, and the random noise source causes a weak secular growth of the field and kinetic energies.

Figure 5 shows results from simulations of laser absorption in a density gradient in two spatial dimensions with the PSC code including the decen-

tering parameter ϵ_2 in the equations of motion. These simulations model the interaction of a semi-infinite laser pulse with a short rise time of 30 fs and a peak intensity of 10^{20}W/cm^2 with a short plasma density gradient and a peak density of $100n_c$. The simulations were performed at a resolution of 50 cells per wavelength and 100 particles per cell. The electron density climbs from vacuum to $100n_c$. The PSC results with $\epsilon_2 = 0$ and 0.02 are much the same, but with $\epsilon_2 = 0.08$ there are significant discrepancies in the results compared to the other two simulations suggesting that there is too much numerical dissipation with $\epsilon_2 = 0.08$.

The analysis of the high-density model equations indicates that the finite-difference equations support an odd-even oscillation if the integration scheme is centered, and this mode is damped if properly decentered. There is no strong evidence of a persistent growing odd-even oscillation in the numerical integrations of the model equations with a noise source included when the equations are centered or when the equations are slightly decentered, although a transient excursion in the electric field energy is observed in Fig. 3 when the scheme is centered. We have shown that a small amount of decentering can be included in the PSC particle pusher with no effect on the simulation results.

We next address some of the electromagnetic modes supported by the finite-difference equations. Consider the simplest fluid analysis of Eqs.(2,6,7) and the linearized cold-plasma fluid equations of motion for fields and fluid quantities $(v_x, v_y, E_x, E_y, B_x, B_y, J_x, J_y)$ with wave propagation $\mathbf{k} = k_z\hat{\mathbf{z}}$ and uniform background magnetic field $\mathbf{B}_0 = B_0\hat{\mathbf{z}}$. The reduced Ampere's law and Faraday's law yield:

$$\nabla \times \nabla \times \mathbf{E} = k_z^2\mathbf{E} = -\frac{1}{c}\frac{\partial}{\partial t}\nabla \times \mathbf{B} = -\frac{4\pi}{c^2}\frac{\partial}{\partial t}\mathbf{J} \tag{29}$$

Multiplying the linearized electron and ion cold-fluid equations for $Z = 1$ by the number density n_0 and adding them with the electron inertia and collisions neglected, we obtain

$$n_0 m_i \frac{\partial}{\partial t}\mathbf{v}_i = e n_0(\mathbf{v}_i - \mathbf{v}_e) \times \mathbf{B}_0/c \rightarrow \mathbf{J} = \frac{c\mathbf{B}_0}{B_0^2} \times n_0 m_i \frac{\partial}{\partial t}\mathbf{v}_i \tag{30}$$

We next substitute the expression for $\mathbf{J}$ from Eq.(30) in Eq.(29) to obtain one equation for the electric field $\mathbf{E}$. A second equation for the electric field is deduced from the ion equation of motion: $\mathbf{E} = -\mathbf{v}_i \times \mathbf{B}_0/c + (m_i/e)\partial\mathbf{v}_i/\partial t$.

Equating the two expressions for $\mathbf{E}$ and Fourier analyzing in time, $-i\omega = \partial/\partial t$, we obtain the following vector equation:

$$[(-\alpha\frac{\omega^2}{\Omega_i} + \Omega_i)v_{y,i} + i\omega v_{x,i}]\hat{\mathbf{x}} + [i\omega v_{y,i} + (\alpha\frac{\omega^2}{\Omega_i} - \Omega_i)v_{x,i})]\hat{\mathbf{y}} = 0 \tag{31}$$

where $\alpha = \omega_{pi}^2/k_z^2c^2$ and $\Omega_i = eB_0/m_ic$ is the ion cyclotron frequency. The determinant of the velocity coefficients in Eq.(31) yields the following dispersion relation:

$$(\alpha\frac{\omega^2}{\Omega_i} - \Omega_i)^2 - \omega^2 = 0 \tag{32}$$

The dispersion relation in Eq.(32) yields Alfvén waves at long wavelengths and low frequency, $\omega = \pm k_z v_a = \pm k_z c\Omega_i/\omega_{pi}$ for $\omega << \Omega_i$, and whistler waves at short wavelengths and high frequencies, $\omega = \pm(k_z^2c^2/\omega_{pi}^2)\Omega_i$ for $\omega >> \Omega_i$. The whistler mode having the higher frequency sets the more stringent constraint on the time step required for stability using an explicit time integration. We can write the stability condition as

$$|\omega\Delta t| = (k_z\Delta z)^2\frac{c^2}{\omega_{pe}^2\Delta z^2}\frac{\Omega_e}{\omega_0}\omega_0\Delta t < O(1) \tag{33}$$

where $\Omega_e = eB_0/m_ec$ is the electron cyclotron frequency. Based on experience in simulations of fast ignition [12], we estimate that $\Omega_e/\omega_0 < O(1)$. In order that the explicit solution of Maxwell's equations remain well behaved at the highest density in the low-density region, then $c/\omega_{pe}\Delta z \geq O(1)$. We also have $k_z\Delta z \leq \pi$. If the transition from the full Maxwell equations to the high-density equations occurs at $100n_c$, *i.e.*, $\omega_{pe}^2/\omega_0^2 = 100$, then $\omega_0\Delta t < 0.1$ is required for stability and needed for accuracy; and the inequality in Eq.(33) is also satisfied.

Now consider the situation when electron-ion collisions are included in the electromagnetic modes at plasma densities exceeding $100n_c$ with a negligible applied magnetic field ($B_0 \approx 0$). Adding the electron and ion equations of motion in the cold-fluid limit, one obtains $n_0m_i\partial\mathbf{v}_i/\partial t = (m_e/e)\nu_{ei}\mathbf{J}$, from which we solve for $\mathbf{J}$. We then use Eq.(29) to determine $\mathbf{E}$ as before and use the alternative equation for $\mathbf{E}$ from the ion equation of motion previously obtained to arrive at a dispersion relation. At these high densities and for relatively cold background electron temperatures, $\nu_{ei} >> \Omega_e$, the dispersion relation yields a damped electromagnetic mode:

$$\omega = -i\frac{k_z^2c^2}{\omega_{pe}^2}\nu_{ei} \tag{34}$$

We note that the right side of Eq.(34) is not a function of density, except for $\ln\Lambda$ in the collision frequency. Analysis of the difference equations for this mode yields $\sin(\omega\Delta t) = -i\frac{k_z^2c^2}{\omega_{pe}^2}\nu_{ei}\Delta t$, and the right side of this equation must be less than unity in magnitude so that the explicit integration of the finite-difference equations remains stable for this damped electromagnetic mode. The stability condition is then

$$(k_z\Delta z)^2\frac{c^2}{\omega_{pe}^2\Delta x^2}\nu_{ei}\Delta t < 1 \tag{35}$$

It is convenient to evaluate this condition at the transition between the low and high-density regions, *e.g.*, $100n_c$, in which case $c^2/\omega_{pe}^2\Delta x^2 = O(1)$. Then Eq.(35) is equivalent to $\nu_{ei}\Delta t < O(1)(k_z\Delta z)^{-2} < O(1/\pi^2)$ at $100n_c$.

In addition to the time-step constraints described in the preceding in the high-density plasma where the Ohm's law is used, deduced from or given by Eqs.(27), (33), (34), and (35), we must still resolve electron and ion motion across the grid, $v\Delta t/\Delta x < 1$, the electron cyclotron motion $\Omega_e\Delta t < 1$, and the collision frequencies for the fast electrons and the background electrons and ions, for sake of accuracy and stability of the simulation. The accuracy constraints on the electron-electron, electron-ion, and ion-ion collisions of the background plasma persist in the high-density region. The electron-ion collisions have to be computed with sufficient accuracy so that these collisions are self-consistent with the resistivity in the Ohm's law. We are investigating how to compute the collisions in the background plasma efficiently but with sufficient accuracy. Subcycling the collisions is one option or we may use simplified collision operators exploiting that the background ions and cold electrons remain close to thermal equilibrium at high collisionalities. The plasma frequency does not have to be resolved in the high-density region. The gradient lengths of the fields and the plasma must be resolved by the grid in the high-density region but not the skin depth nor the Debye length. However, all of the standard accuracy and stability conditions still apply in the low-density region where the conventional explicit time integration of the complete Maxwell and particle equations is undertaken [1, 31, 32].

The use of the reduced magnetohydrodynamic equations in the high-density region is justified because the reduced equations yield the same results for problems of interest as the solution of the complete Maxwell's equations for the electric and magnetic fields in the transition region where the plasma has become relatively collisional. The solution for the electric field

is reasonably continuous. If the electric field is continuous and smooth, then Faraday's law will generate relatively continuous magnetic fields across the interface. The PIC and complete Maxwell equations solution in the low-density region suffers more from particle noise than does the solution of the reduced equations (the latter set has eliminated electron plasma waves and light waves, so its thermal fluctuation level is inherently lower [1, 3, 24]). We have experimented with spatial smoothing of the computed electric field across the transition boundary in case it is needed. So far in our two-region extension of the PSC, we have not had to do any spatial smoothing of the electric field across the boundary between the low and high-density regions (although we digitally smooth the electric and magnetic field in the high-density region) nor have we had to decenter the PIC equations of motion to control an odd-even oscillation. In our test-bed computations using the model equations given in the preceding, we have had good success with the following two simple spatial smoothing algorithms.

The first smoothing scheme consists of iterating the following relation

$$\mathbf{E}_j^{(r+1)} = \frac{1}{4}(\mathbf{E}_{j-1}^{(r)} + 2\mathbf{E}_j^{(r)} + \mathbf{E}_{j+1}^{(r)}) \tag{36}$$

over an interval surrounding the boundary between the low and high-density regions, where r indicates the iteration level and the subscript j indicates the spatial grid index. In practice, we limit the number of iterations to a small integer. We have used intervals from three cells on either side of the interface to the entire overdense domain and obtained good results.

A second spatial smoothing scheme worked equally well:

$$\mathbf{E}_j = \beta\mathbf{E}_j^I + (1-\beta)\mathbf{E}_j^{II} \tag{37}$$

where $\beta = (i - \Delta L/2\Delta x - j)/\Delta L$, ΔL is the interpolation interval, i is the grid cell index denoting the boundary between the low (I) and high (II) density regions, $i - \Delta L/2\Delta x \le j \le i + \Delta L/2\Delta x$, and $\mathbf{E}^{I,II}$ is the electric field determined by the low/high-density field equations. In this second smoothing scheme the electric field is solved using the equations of region I for $j \le i + \Delta L/2\Delta x$ and the equations of region II for $j \ge i - \Delta L/2\Delta x$.

Figure 6 shows the results of integrating the model finite-difference equations for propagation of a linearly polarized electromagnetic wave (E_y, B_x) into a density gradient with a very weak noise source in the plasma current using the first smoothing scheme with just a single pass of the smoothing operator. In addition, we have included the displacement current as described

in Eqs.(9-11) We display B_x and E_z vs. z at $t = 125$ where the boundary between the regions is at $z = 37.5$ with parameters $e/m_e = c = \omega_0 = 1$, $\Delta t = 0.025$, $\Delta z = 0.05$, system length $L_z = 50$, $\Delta L = 40\Delta x$, incident wave amplitude in vacuum $B_{x0} = 0.01$, noise amplitude in the plasma currents 10^{-10}, suppressing electron inertia and electron pressure in the Ohm's law for the background electrons, and with spatial variation of the electron plasma frequency and electron-ion collision frequency as shown in Figure 6a. Both smoothing schemes obtained much the same results which differ negligibly from doing no smoothing or interpolation of the electric field across the interface between the regions.

This section of the paper has presented an analysis of the time-integration characteristics of the reduced physics model used in the high-density region, described an extension that includes the displacement current in Ampere's law, discussed two smoothing schemes for the electric field, and illustrated some of the algorithmic issues in a simplified testbed model. The reduced physics model in the high-density region removes light waves and electron plasma waves; the electromagnetic skin depth and electron Debye length do not have to be resolved by the spatial mesh; and the time step is not constrained by the electron plasma frequency in the high-density region. The simulations presented in the next section illustrate that the new PIC-hybrid framework can achieve a large computational savings by allowing the use of larger time steps and a larger spatial grid cell widths, which then allows the use of fewer total particles for a system with the same physical dimensions while maintaining the same number of particles per cell.

4. PSC Simulations

We have extended the PSC code into a prototype two-region code and undertaken one-dimensional (1D) and two-dimensional (2D) simulations to test the new composite simulation framework. First we report experience with a few 1D simulations. The 1D simulation undertaken with PSC (full Maxwell equations and no two-region extension) shown in Fig. 2 is used as a benchmark for simulations with the two-region, extended PSC+ code. In this simulation a laser pulse is propagated into a plasma density gradient. The parameters for this 1D simulation are described in Sec. 2. The interface between the complete Maxwell equations solver and the high-density field solver based on Ohm's law is located at the point where the initial density profile reaches $90n_c$, approximately at 9 microns. The PIC two-region sim-

ulation was performed at a resolution of 100 cells per wavelength, 100 ion particles per cell, and 400 electron particles per cell ($Z = 4$ for copper). With 200 cells per micron (cpm), 100 ion particles per cell, and 400 electron particles per cell, PSC required 64 cpus and 2 hours of wall clock time to do the simulation in Fig. 2. The computations increase linearly with the total number of cells for fixed number of particles per cell and fixed time step, and become impractically large in 2D and 3D if we want to undertake many simulations, each with reasonably short turnaround times. In the 1D PSC simulations we pick a static boundary between the low-density and high-density regions. In the 2D PSC simulations the boundary between the two regions is again static, and the boundary is planar (a constant density surface at the beginning of the simulation). The electric field is determined up to and including the boundary by the low-density Maxwell-PIC equations, and the electric field in the high-density region is determined by Ohm's law omitting the gradient of the electron pressure and the momentum exchange term with the fast electrons. In 2D the $\mathbf{v_e} \times \mathbf{B}$ term is retained on the right side of the Ohm's law, but not in 1D. So far we have not employed any of the spatial smoothing algorithms operating on the electric field across the low to high-density interface described in Sec. 3 in the PSC simulations. For the magnetic fields in the high-density region that arise in the 2D simulations, we find that $\Omega_e \tau_{ei} << 1$, for which the Braginskii resistivity is a scalar (Sec. 2).

We have undertaken two 1D two-region PSC simulations (Fig. 7) with and without the displacement current in Ampere's law in the high-density region. The displacement current is retained in the high-density region of the 2D two-region hybrid simulations with the $\mathbf{v_e} \times \mathbf{B}$ term in Ohm's law determined directly from the electron particle mean velocity accumulated on the grid. The electron density used in Ohm's law in the high-density region in this simulation is computed either directly from the electron particle data or from the electron particle data with a current correction to enforce consistency with Ampere's law, Eq.(7). In 1D the current correction is calculated by adding a drift to all of the background electrons in each cell such that the total J_z particle current summed over all species (and time-averaged over three laser cycles to smooth the data) is zero. The electric field, background electron density, and electron temperature are digitally smoothed in the high-density region with a single-pass 1-2-1 filter. The plasma currents used in Maxwell's equations are digitally smoothed over the entire domain similarly. The physics parameters of the two-region PIC-hybrid simulations

are identical to those of the PIC simulation described in Fig. 2. The interface between the low and high-density regions is located at the point where the initial density profile reaches $90n_c$, approximately at 9 microns. The two-region PIC-hybrid simulation was performed at a resolution of 100 cells per wavelength, 100 ion particles per cell, and 400 electron particles per cell. Figure 7a shows the comparison of PSC and two-region PSC+ for 100 cpm. The electric fields vs. z at 93 fs agree well with one another and with the $E_z = \eta J_z^b$ relation. Recall that J_z^b is the current carried by the background electrons and ions excluding the fast electron current. We note that the electron density climbs to $360n_c$ for which $\nu_{ei}\Delta t > 1$. The noise reduction in the high-density region in the two-region simulation is dramatic.

Figure 7b shows the comparison of the longitudinal electric field E_z vs. z in the two two-region PSC+ simulations with n_e in Ohm's law determined directly from the electron particle data with no current correction, and with 100 particles per cell per species and 20 cells per micron or 100 cells per micron throughout. The boundary between the low and high-density regions in the two-region simulations was taken at 9μm for 100 cpm and 7μm for 20 cpm. As the spatial resolution decreases, the time step is increased so that the Courant conditions are maintained. However, this forces the boundary between the low and high-density regions to shift to lower density to limit the maximum value of $\omega_{pe}\Delta t < O(1)$ to maintain stability and accuracy in the low-density side of the simulation. The electric fields compare very well. With the five-fold increased time step and five-fold decreased number of cells and particles, the 1D two-region simulation for 20 cpm should be at least 25× faster (the operations count in the simulation scales linearly in the product of the number of time steps times the number of particles, excluding considerations of the binary collisions whose computational scaling is stronger than linear). In 2D the simulation is expected to run at least $5^3 = 125\times$ faster and more than 625× faster in 3D compared to using the conventional PSC code if the physical time and spatial dimensions are held fixed. Because the binary collisions are a large contributor to the operations count, a larger savings in run time is in fact realized for a five-fold reduction in spatial resolution per spatial dimension with fixed number of particles per cell because of the particle sorting required in the binary collision algorithm.

In Figs. 8 and 9 we compare three 1D PSC simulations using the same parameters as in Fig. 7a: full PIC (same simulation used in Fig. 7a), two-region hybrid model with n_e computed directly from the particle electrons, and two-region hybrid model with the displacement current retained as in

Eq.(9) and n_e computed directly from the particle electrons with a current correction made to ensure consistency with Ampere's law. Plots of E_z, ηJ_z^b, T_e, and n_e vs. z are shown from the three simulations in Fig. 8. Diagnostic plots of J_e^f and the total particle J_z vs. z from the three simulations are shown in Fig. 9. We do not compare the ion temperatures as the results for the ion dynamics showed negligible differences. We note that the E_z, ηJ_z^b, J_z^f, T_e, and n_e data differ very little in the three simulations, although E_z in the low-density region is relatively noisy and there is noise in E_z at high density in full PIC. The total J_z diagnostic in the high-density region shows the most significant differences between the three simulations. It is important to note that the two-region model in 1D invokes $J_z = 0$ in the high-density region if the displacement current is omitted and $4\pi J_z = -\partial E_z/\partial t$ if the displacement current is retained. We also note that in the full-PIC simulation in the high-density region $J_z = 0$ to very good approximation implying that the displacement current $\partial E_z/\partial t$ is very small (Fig. 9a), which lends support to the assumptions made in the hybrid model. Because the displacement current is small in the high-density region, it is sufficient that the current correction used in the third simulation tries to recover $J_z = 0$ which is equivalent to satisfying Eq.(8), because the difference between $J_z = 0$ and $4\pi J_z = -\partial E_z/\partial t$ is small. While the total J_z particle current in Fig. 9b is small compared to J_e^f in the high-density region, the total J_z particle current in the high-density region in Fig. 9c, which includes the current correction, is even smaller; and a better approximation to the full PIC results is achieved. We conclude that using n_e directly from the particle electrons in the Ohm's law without the current correction to enforce consistency with Ampere's law leads to inferior results for the two-region hybrid model, although the results in Figs. 7 and 8 are not much affected by the current correction. We note that the total cpu time consumed in the low-resolution 1D PIC-hybrid simulation is $44\times$ smaller than the total cpu time in the high-resolution 1D full PIC simulation for this example.

In Figs. 11-15 we illustrate the extension of the 1D two-region PSC simulation to 2D. We compare 2D full PIC to two-region hybrid PSC simulations at full resolution (100 cpm) and reduced resolution (20 cpm) for a fixed domain size of $30\mu\text{m} \times 30\mu\text{m}$. In the 2D simulations we use 10 ions per cell and 40 electrons per cell. The two-region hybrid simulations include the displacement current and use n_e determined from the particle electrons with current correction for consistency with Ampere's law. The current correction in 2D involves computing the background electron density from the particles after

adding a local vector drift to the background electron velocities in the 2D yz simulation plane so that Eq.(7) is satisfied in the high-density region. The simulation addresses laser propagation, absorption and electron transport for the incident laser pulse with Gaussian transverse profile (6 micron full width at half maximum). In these simulations we used either 100 cpm or 20 cpm and 10 ions per cell/40 electrons per cell modeling a copper plasma. The electric and magnetic fields, background electron density, and electron temperature are digitally smoothed in the high-density region with successive 1D 1-2-1 filtering (single pass) in the two directions. The plasma currents used in Maxwell's equations are digitally smoothed over the entire domain similarly. The electron density climbs to $360n_c$. The other parameters for these simulations are the same as in the 1D simulations described in Fig. 2, 7-9. The density profile is initially uniform in the transverse direction and identical to the 1D profile in the longitudinal direction. The interface between the two regions (full PIC and Maxwell's equations and PIC plus Ohm's law) is static and located where the density exceeds $90n_c$ at $z = 8\mu$m. The laser is incident at $z = 0$, propagates in z, and has a finite spot size in y. We plot n_e in Fig. 10, T_e in Fig. 11, E_z in Fig. 12, B_x in Fig. 13, total J_z in Fig. 14, and the fast electron current J_z^f in Fig. 15, all at at 90 fs. We plot 2D contours and axial line-outs vs. z in the midplane, except for B_x.

The comparisons of the results are generally good, but there are some modest differences in the longitudinal electric fields, the magnetic fields, the electron temperatures, and the longitudinal currents. The PIC-hybrid simulations results for E_z are significantly less noisey in the high-density region than the full PIC results. The numerical noise in the full PIC simulation leading to fluctuations in the electric field of the order of $< E^2 >^{1/2} \approx 0.001\, E_0$ (E_0 and B_0 are the incident electric and magnetic field amplitudes in the laser) cause a rise in the background temperature from 100 eV up to 150 eV even before the arrival of laser-driven electrons. At 90 fs the background electron temperature T_e is slightly higher near the laser beam axis in y for $z > 8\mu$m in the full PIC simulation than in the PIC-hybrid simulations shown in Fig. 11. This reduces the collisionality and the resistivity of the plasma deep in the target, *i.e.*, at $z > 20\,\mu$m at the time shown here. However, the electromagnetic field noise and reduced collisionality affect the transport of the fast electrons very little in the full PIC simulation as compared to the PIC-hybrid simulations in Fig. 15. Numerical self-heating can be mitigated by higher-order particle shape functions or increased number of particles per cell, both of which are beyond the scope of the present study. In contrast,

the numerical noise level in the PIC-hybrid simulation is lower, on the order of $10^{-4}\,E_0$.

In Fig. 11 there is a difference in the electron temperature profile at low densities and well off the axis in z determined by the centroid of the incident laser in the low-resolution simulation results shown in Fig. 11c compared to the results in Figs. 11a and 11b. Both the high and low-resolution simulations exhibit some numerical heating of the electron velocity distributions in the low-density full-PIC regions of the simulations. In the low-resolution simulation the resolution of the electron Debye length and the statistical resolution are less than in the high-resolution cases, which fact makes the numerical heating of the electron velocity distribution somewhat stronger in the full-PIC simulation region of Fig. 11c. We think that this contributes to the difference observed in the side lobes of the electron temperature profile in Fig. 11c compared to the profiles in Figs. 11a and 11b. If significant numerical heating is occurring in the full-PIC region of the PIC-hybrid simulations, this can be mitigated by using a higher spatial resolution only in the full-PIC low-density region; the efficacy of this strategy will be studied in future work.

There are also differences in the small magnetic fields that arise at densities $n_e > n_c$ in the full PIC and PIC-hybrid simulations (Fig. 13). On the high-density side of the interface between the low and high-density models, there is a small axial magnetic field $B_x \approx 0.01 B_0$ located in the density ramp before the plateau (see Fig. 13b,c). A similar magnetic field is also present in the collisional PIC run, but lower in magnitude and slightly different in shape, and somewhat obscured by noise, see Fig. 13a. This difference between the two simulation approaches can be explained by differences in the profile of the plasma electrical resistivity which is involved in relating the fast current generated in the laser interaction with the electric field in the PIC-hybrid region through Ohm's law. The plasma resistivity is related to the plasma temperature via $\eta \propto T^{-3/2}$, which explains how stronger heating in the density gradient between $90 - 360\,n_c$ in the PIC simulation allows less magnetic field formation (T_e is slightly larger which makes the resistivity smaller; and $\mathbf{E}$ from Ohm's law is smaller in consequence, which then makes $\mathbf{B}$ smaller as a result of Faraday's law). Laser-induced heating of the density gradient eventually slows the magnetic field growth even in the PIC-hybrid simulation. In any case, the magnitude of the magnetic fields and the narrowness of the magnetic field layer suggest that the differences in the simulation outcomes due to the effects of the magnetic field are negligible here.

In the plasma at higher density than in the density-ramp region, the electron density and the resistivity are relatively constant; and the curl of the electric field more nearly cancels, which through Faraday's law forces the magnetic field to remain small. The smallness of the magnetic field in turn forces the curl of the magnetic field and the total current to be small given that the displacement current is also small. However, in the density-ramp region, the gradients of the electron density and the resistivity due to the temperature gradient allow the curl of $\mathbf{E} = \eta \mathbf{J}^b$ to be finite, which allows a small magnetic field to be generated.

In Figs. 14e and 14f we note that the total J_z current in the reduced resolution PIC-hybrid simulation is not as close to zero in the high-density region as in Figs. 14a-14d that show the total current in the full PIC and PIC-hybrid simulations at full resolution. By doing additional simulations we have determined that the value of J_z in the high-density region in the low-resolution simulation is reduced if the rise time of the laser (artificially short in the simulation) is better resolved by the time step, which then improves the statistics in the lag average of the axial current used in correcting the background electron density in the high-density physics model.

The two PIC-hybrid simulations at the two resolutions agree with one another relatively well. The full PIC and PIC-hybrid PSC two-dimensional simulations at full resolution required approximately 30,000 CPU hours, while the PIC-hybrid simulation at reduced resolution required less than an hour on 64 processors, which gave $> 500\times$ reduction in the computational cost.

We have begun to apply the new framework introduced here to the study of diverse physics applications addressing the physics of fast ignition, which will be reported elsewhere. We believe that the noise reduction in the PIC-hybrid simulations is an advantage over the full PIC simulations. However, more research is needed on what is the physically correct thermal noise level and how to simulate it in a particle or hybrid code for conditions in which $n_e \lambda_e^3$ is less than unity at high-densities for a given electron temperature. We acknowledge that there is more work to be done in understanding the fidelity of both the full PIC and PIC-hybrid simulations, in controlling the particle noise in the full-PIC simulation domains, in comparing the full PIC and PIC-hybrid simulations, and in optimizing the PIC-hybrid framework.

5. Summary and Conclusions

We have introduced a new framework for simulating the physics of short-pulse laser-plasma interactions of intense pulses at spatial and temporal scales relevant to experiments, using a new approach that combines a multi-dimensional collisional electromagnetic PIC code with a reduced model of high-density plasma based on Ohm's law. In the latter, collisions damp out plasma waves so that electron inertia in the background electrons and the displacement current are unimportant; and an Ohm's law with electron inertia effects neglected determines the electric field. In addition to yielding orders of magnitude in speed-up while avoiding numerical instabilities, this allows us to model many aspects of fast-ignition laser plasma interactions and fast-electron transport in a single unified framework: the laser-plasma interaction at sub-critical densities, energy deposition at relativistic critical densities, and fast-electron transport at high densities. We hope to address key questions such as the multi-picosecond temporal evolution of the laser-energy conversion into hot electrons, the impact of return currents on the laser-plasma interaction, the effects of resistive heating in the plasma, and the effects of self-generated electric and magnetic fields on electron transport with the framework introduced here.

We have reported 1D and 2D applications that illustrate the algorithm and its ability to simulate fast-igntion physics. We compare simulations using full PIC to those using the two-region PIC-hybrid framework. The use of the two-region algorithm relaxes the requirements on spatial and temporal resolution over conventional PIC simulation using finite-difference methods and explicit time integration of the complete set of Maxwell's equations. By allowing the use of a coarser spatial mesh, the total number of particles can be reduced, which leads to a significant computational savings. The improvements in run time for the same physical simulation increase with the number of spatial dimensions: we achieve a reduction in computer run time that is $> 40\times$ in our reduced-resolution 1D PIC-hybrid simulation example and $> 500\times$ shorter in our 2D PIC-hybrid simulation example as compared to the full PIC simulations at higher resolution for the same problem.

In the model equations and the simulations presented here, we have frozen the location of the boundary between the low and high-density plasma domains. However, making the location of this boundary static is not required; and we are undertaking simulations in which the boundary moves to higher density if the background plasma heats, *i.e.*, the location of the boundary

becomes adaptive. In general, the boundary location should evolve and migrate to either higher or lower density if the plasma heats or cools, respectively. What matters in determining the location of the boundary is that the high-density plasma is defined by the electron collision frequency being a significant fraction of the electron plasma frequency. Moreover, the boundary is not required to be a line in two dimensions or a plane in three dimensions.

Although our two-region algorithm significantly relaxes constraints on time step, grid size, and particle number, there are residual requirements on spatial and temporal resolution. An important question is how accurate a representation is needed for the collision effects in the high-density, resistive, background plasma, because the computational burden of calculating the collisions in a particle simulation is significant. We will give this issue more attention in future work. There are other physics and numerical considerations that affect the new framework introduced here: these are not fully settled and also will receive more attention in future work.

We acknowledge valuable input and encouragement from D. Larson, M. Tabak, R. Town, M. Key, P. Patel, D. Strozzi, A. Friedman, and R. Cohen. We also appreciate useful discussions with W. Mori and J. Tonge. This work was performed under the auspices of the U.S. Department of Energy by the Lawrence Livermore National Laboratory under Contract DE-AC52-07NA27344.

References

[1] C. K. Birdsall and A. B. Langdon, *Plasma Physics Via Computer Simulation* (McGraw-Hill, New York, 1985).

[2] R. W. Hockney and J. W. Eastwood, *Computer Simulation Using Particles* (McGraw-Hill, New York, 1981).

[3] J. U. Brackbill and B. I. Cohen, *Multiple Time Scales* (Academic Press, San Diego, 1985).

[4] M. Tabak *et al.*, Phys Plasmas **1**, 1626 (1994).

[5] S. C. Wilks and W. L. Kruer, IEEE Journal of Quantum Electronics **33**, 1954 (1998).

[6] B. F. Lasinski *et al.*, Phys. Plasmas **6**, 2041 (1999).

[7] A. J. Kemp, Y. Sentoku, and M. Tabak, Phys. Rev. Lett. **101**, 4075004 (2008).

[8] B. F. Lasinski *et al.*, Phys. Plasmas **16**, 012705 (2009).

[9] M. E. Glinsky, Phys. Plasmas **2**, 2796 (1995).

[10] J. R. Davies, Phys. Rev. E **65**, 026407 (2002).

[11] L. Gremillet, G. Bonnaud, and F. Amiranoff, Phys. Plasmas **9**, 941 (2002).

[12] J. J. Honrubia and J. Meyer-ter-Vehn, Plas. Phys. Contr. Fusion **51**, 014008 (2009).

[13] Y. Sentoku and A. Kemp, J. Comput. Phys. **227**, 6846 (2008).

[14] A. Friedman, A. B. Langdon, and B. I. Cohen, Com. Plas. Phys. Contr. Fusion **6**, 225 (1981).

[15] R. J. Mason, in *Multiple Time Scales*, edited by J. U. Brackbill and B. I. Cohen (Academic Press, San Diego, 1985), Chap. 8.

[16] J. U. Brackbill and D. W. Forslund, in *Multiple Time Scales*, edited by J. U. Brackbill and B. I. Cohen (Academic Press, San Diego, 1985), Chap. 9.

[17] A. B. Langdon, B. I. Cohen, and A. Friedman, J. Comput. Phys. **51**, 107 (1983).

[18] B. I. Cohen, A. B. Langdon, and A. Friedman, J. Comput. Phys. **46**, 15 (1982).

[19] T. P. Hughes, R. E. Clark, and S. S. Yu, Phys. Rev. Spec. Topics Accel. Beams **2**, 110401 (1999).

[20] D. R. Welch, D. V. Rose, B. V. Oliver, and R. E. Clark, Nucl. Instr. Meth. Phys. Res. A **464**, 134 (2001).

[21] P. Degond, F. Deluzet, and L. Navoret, C. R. Acad. Sci. Paris, Ser. I **343**, 613 (2006).

[22] R. J. Mason, J. Comput. Phys. **71**, 429 (1987).

[23] B. I. Cohen, A. B. Langdon, D. W. Hewett, and R. J. Procassini, J. Comput. Phys. **81**, 151 (1989).

[24] A. B. Langdon and D. C. Barnes, in *Multiple Time Scales*, edited by J. U. Brackbill and B. I. Cohen (Academic Press, San Diego, 1985), Chap. 11.

[25] D. W. Hewett and C. W. Nielson, J. Comput. Phys. **29**, 219 (1978).

[26] B. I. Cohen, J. A. Byers, W. C. Condit, and J. D. Hanson, J. Comput. Phys. **27**, 363 (1978).

[27] D. W. Hewett, J. Comput. Phys. **38**, 378 (1980).

[28] D. Winske, Physica D: Nonlinear Phenomena **77**, 268 (1994).

[29] T. Taguchi, T. M. Antonsen, C. S. Liu, and K. Mima, Phys. Rev. Lett. **86**, 5055 (2001).

[30] J. Denavit, J. Comput. Phys. **42**, 337 (1981).

[31] A. J. Kemp and H. Ruhl, Phys. Plasmas **12**, 033105 (2005).

[32] M. Bonitz, G. Bertsch, V. S. Filinov, and H. Ruhl, *Introduction to Computational Methods in Many Body Physics* (Rinton Press, Princeton, NJ, 2006), Vol. ISBN 1-58949-009-6, Chap. 2.

[33] B. Marder, J. Comput. Phys. **68**, 48 (1987).

[34] A. B. Langdon, Comput. Phys. Commun. **70**, 447 (1992).

[35] S. I. Braginskii, in *Reviews of Plasma Physics*, edited by M. A. Leontovich (Consultants Bureau, New York, 1965), Vol. 1, p. 205.

[36] E. M. Epperlein and M. G. Haines, Phys. Fluids **29**, 1029 (1986)).

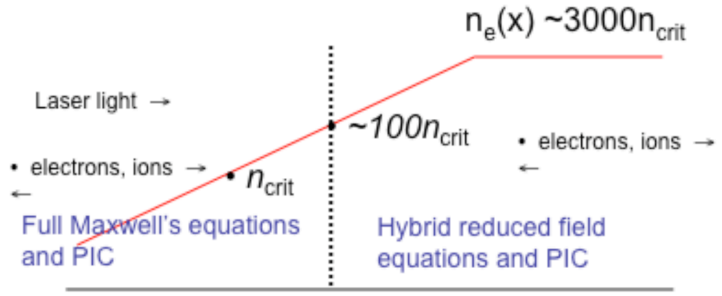

Figure 1: Schematic of plasma density gradient showing the low and high-density regions in which different field equations are used. (color online)

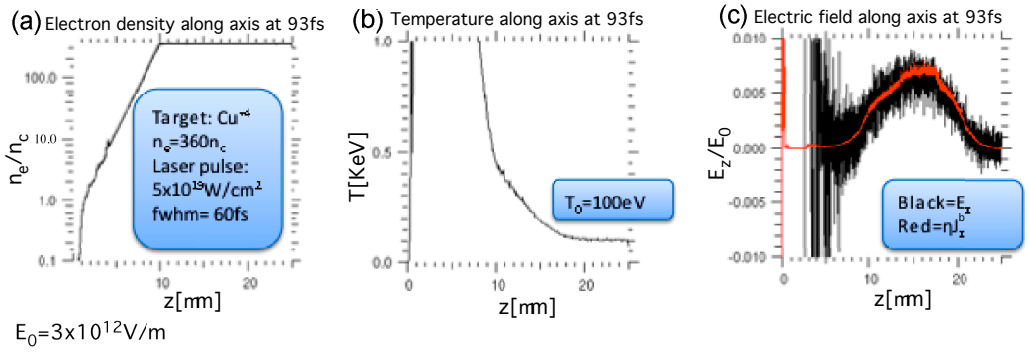

Figure 2: One-dimensional PSC conventional PIC simulation of laser absorption in a plasma density gradient.(a) Plasma density gradient.(b) Electron temperature at 93.348 fs vs. z with initial background temperature 100eV.(c) Longitudinal electric field E_z vs. z at 93.348 fs shown in black with ηJ_z^b shown in red. (color online).

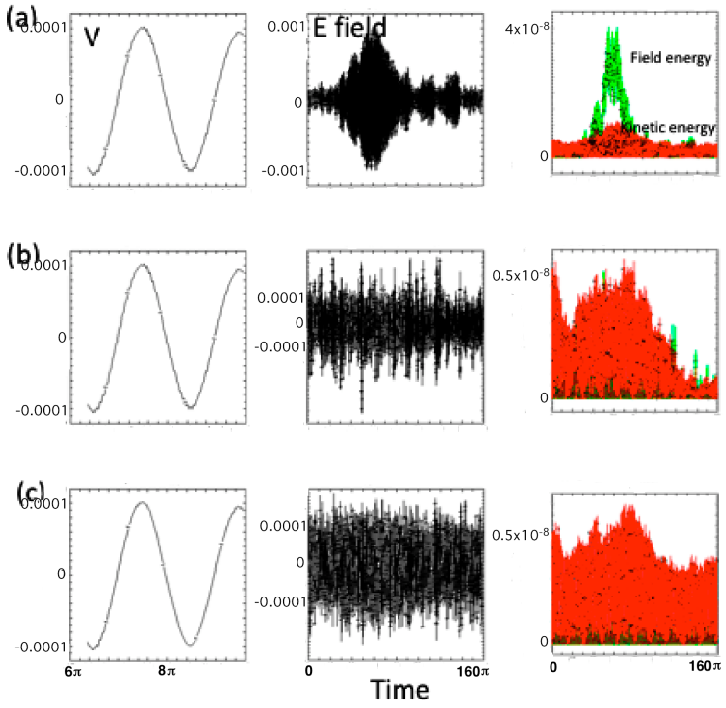

Figure 3: Integration of model difference equations for ion accoustic waves with $kc_s\Delta t = 0.1$ showing the fluid velocity vs. time in units such that a wave period equals 2π, electric field vs. time (80 periods), and the electric field and kinetic energy integrals over the volume vs. time (80 periods). (a) $\epsilon_1 = \epsilon_2 = 0$, $\nu = 0$, and $N_f = \infty$.(b) $\epsilon_1 = \epsilon_2 = 0$, $\nu = 0$, and $N_f = 75$. (c) $\epsilon_1 = \epsilon_2 = 0.02$, $\nu = 0$, and $N_f = \infty$. (color online).

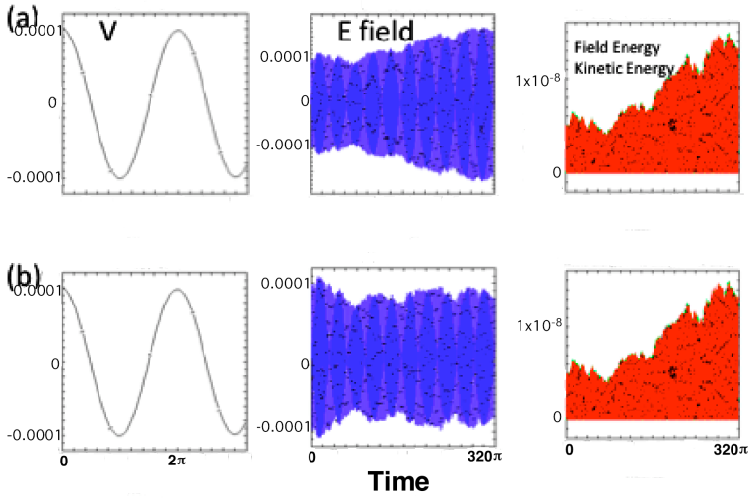

Figure 4: Integration of model difference equations for electron plasma waves with $\omega_{pe}\Delta t = 0.1$ showing the fluid velocity vs. time in units such that a wave period equals 2π, electric field vs. time (160 periods), and the electric field and kinetic energy integrals over the volume vs. time (160 periods). (a) $\epsilon_2 = 0$, $\nu = 0$.(b) $\epsilon_2 = 0.02$, $\nu = 0$ (color online).

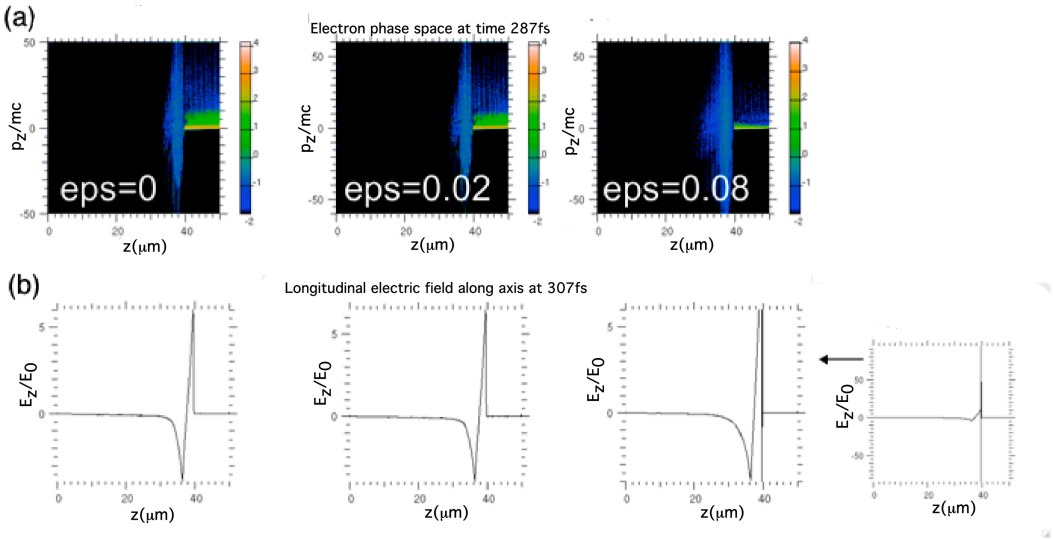

Figure 5: One-dimensional PSC conventional PIC simulation of laser absorption in a plasma density gradient for $\epsilon_2 = 0, 0.02, 0.08$.(a) Electron phase space, momentum $p_z/m_e c$ vs. z at 287 fs .(b) Corresponding electric field vs. z at 307 fs. (color online).

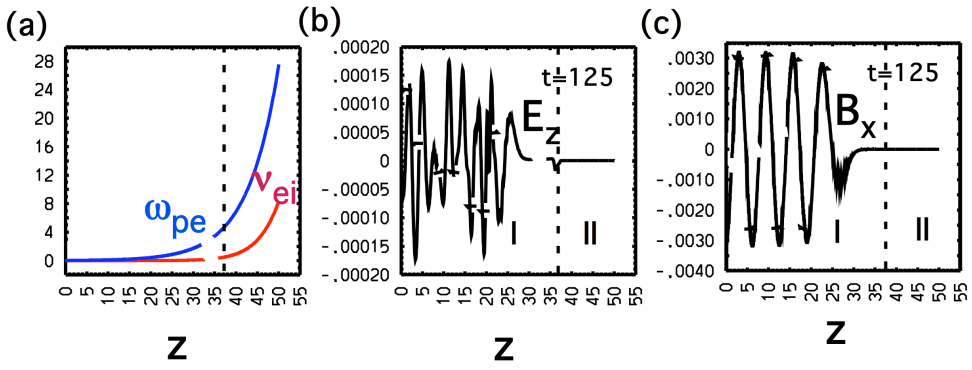

Figure 6: One-dimensional integration of model equations for laser propagation in a plasma density gradient with digital spatial smoothing around the transition from low to high-density regions at $z = 37.5$ over $20\Delta x$ on either side of the interface with units such that $e/m_e = c = \omega_0 = 1$.(a) Plasma frequency ω_{pe} and electron-ion collision frequency ν_{ei} vs. z.(b) Longitudinal electric field E_z vs. z at $t = 125$. (c) Magnetic field B_x vs. z at $t = 125$.

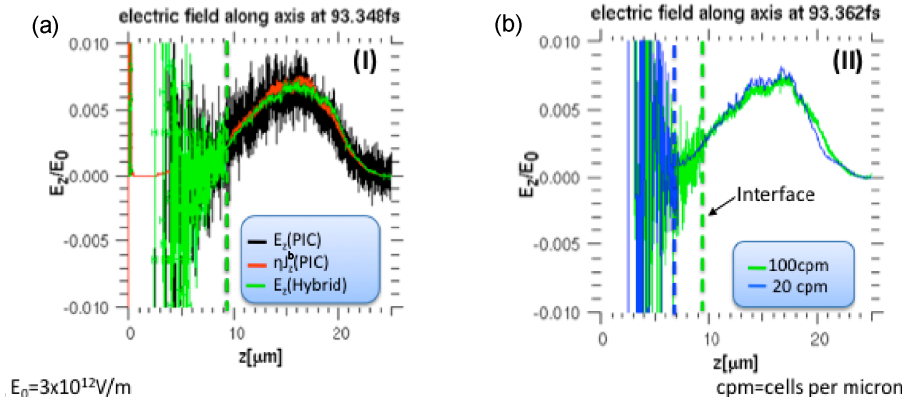

Figure 7: One-dimensional simulations of laser absorption in a plasma density gradient.(a) Electric field E_z vs. z at 93 fs in PSC conventional PIC and two-region extended PSC simulations with 100cpm and 100 particles per cell.(b) Electric field E_z vs. z at 93 fs in two-region extended PSC simulations with 20 cpm and 100 cpm. (color online). J_z^b is the current carried by the background electrons and ions.

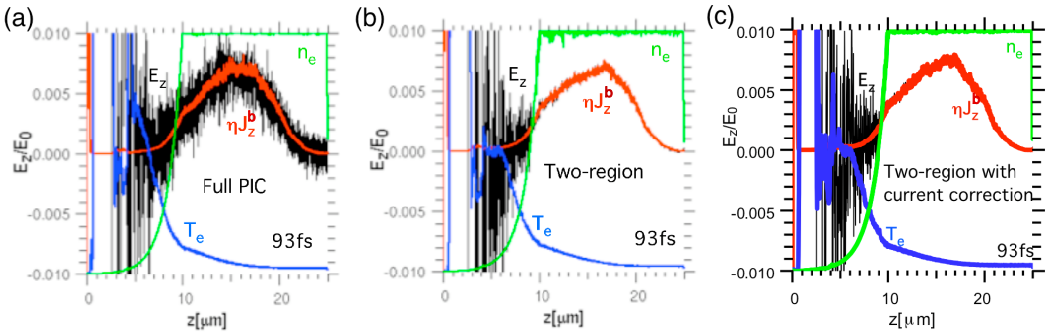

Figure 8: One-dimensional simulations of laser absorption in a plasma density gradient showing the electric field E_z/E_0, and electron temperature T_e and electron density n_e, in arbitrary units at 93 fs with 100cpm and 100 particles per cell: (a) conventional PSC PIC simulation; (b) two-region extended PSC simulation; and (c) two-region extended PSC simulation with electron current correction. (color online).

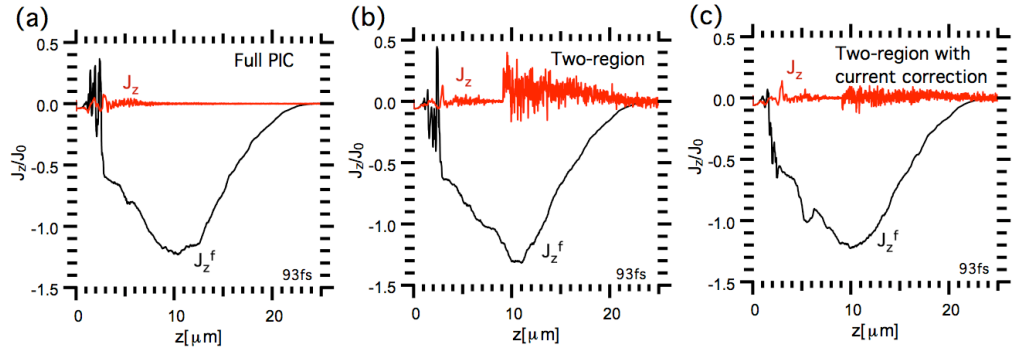

Figure 9: One-dimensional simulations of laser absorption in a plasma density gradient showing the fast electron current J_z^f and the total current J_z, in units of $J_0 = en_c c$ at 93 fs with 100cpm and 100 particles per cell: (a) conventional PSC PIC simulation; (b) two-region extended PSC simulation; and (c) two-region extended PSC simulation with electron current correction. (color online).

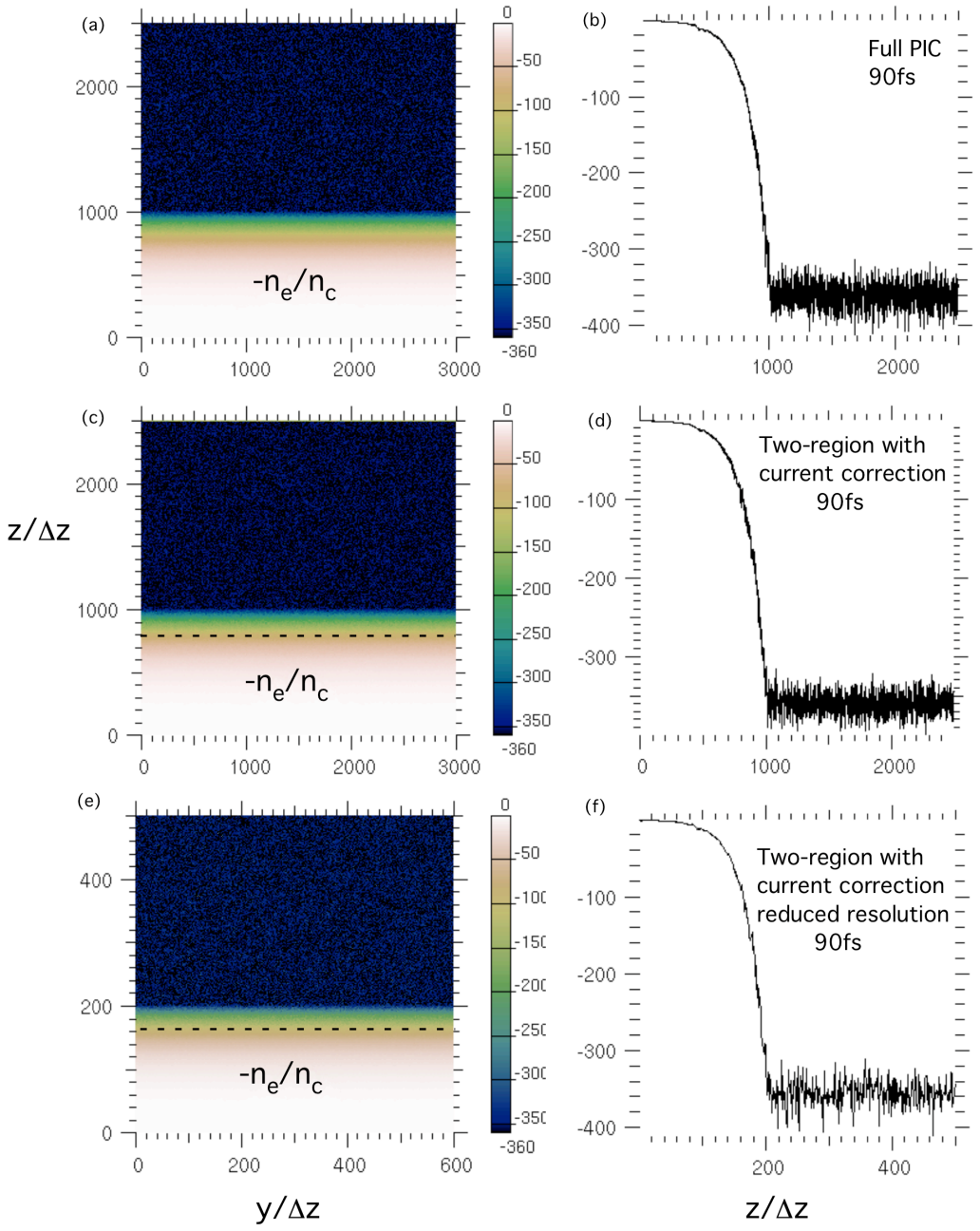

Figure 10: Two-dimensional PSC simulations of laser absorption in a plasma density gradient extending the 1D simulations shown in Figs. 2, 7-9 to 2D: full PIC, two-region PIC-hybrid at full resolution (100 cpm), and two-region PIC-hybrid at reduced resolution (20 cpm) showing 2D contours in (a), (c), and (e) and line-outs in (b), (d), and (f) of n_e vs. z in the midplane at 90fs. The dashed lines in (c) and (e) show the location of the boundary between the low and high-density regions. (color online

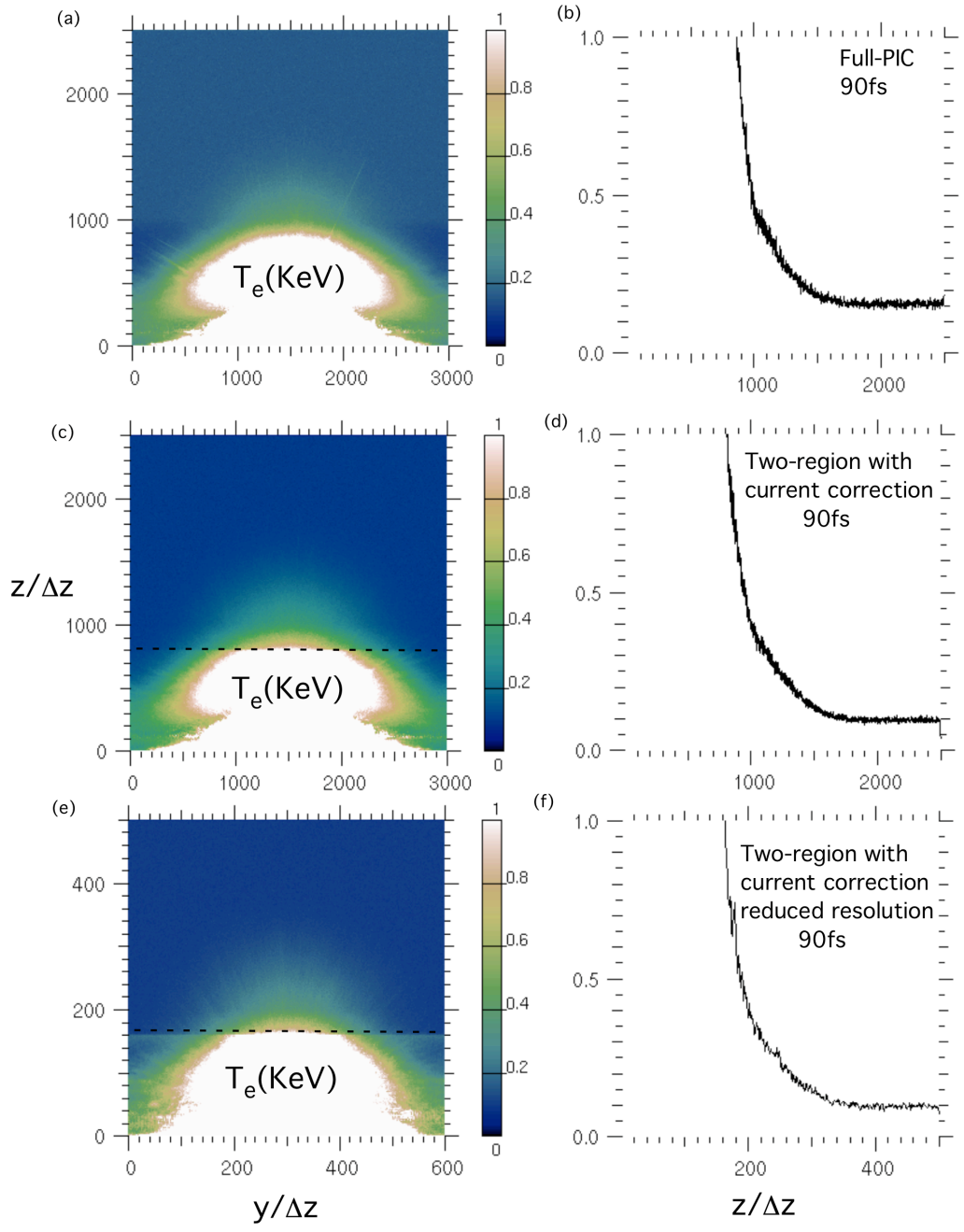

Figure 11: Two-dimensional PSC simulations extending the 1D simulations shown in Figs. 2, 7-9 to 2D: full PIC, two-region PIC-hybrid at full resolution (100 cpm), and two-region PIC-hybrid at reduced resolution (20 cpm) showing 2D contours and line-outs of T_e vs. z in the midplane at 90fs. (color online).

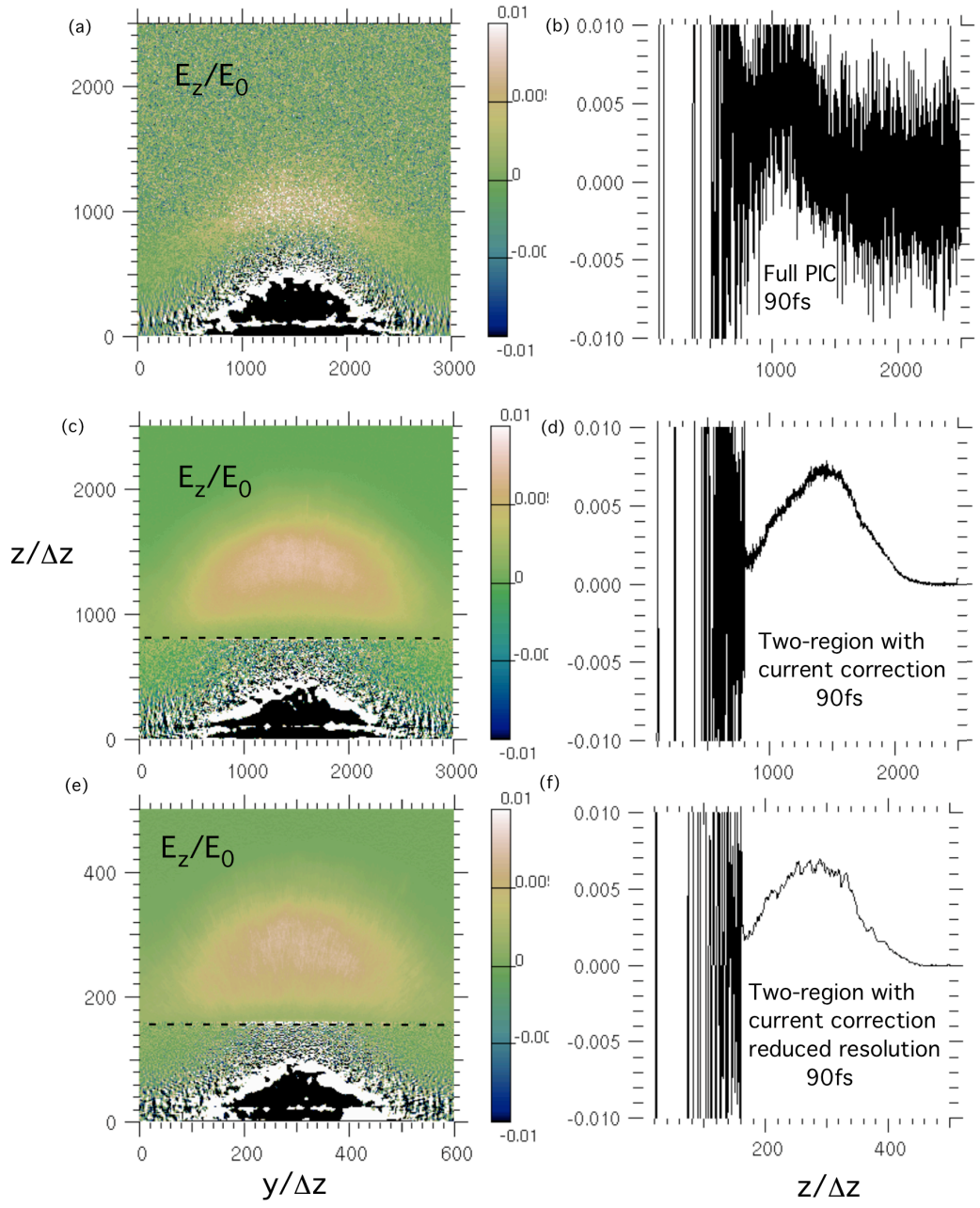

Figure 12: Two-dimensional PSC simulations extending the 1D simulations shown in Figs. 2, 7-9 to 2D: full PIC, two-region PIC-hybrid at full resolution (100 cpm), and two-region PIC-hybrid at reduced resolution (20 cpm) showing 2D contours and line-outs of E_z vs. z in the midplane at 90fs. $E_0 = 3 \times 10^{12}$ V/m.(color online)

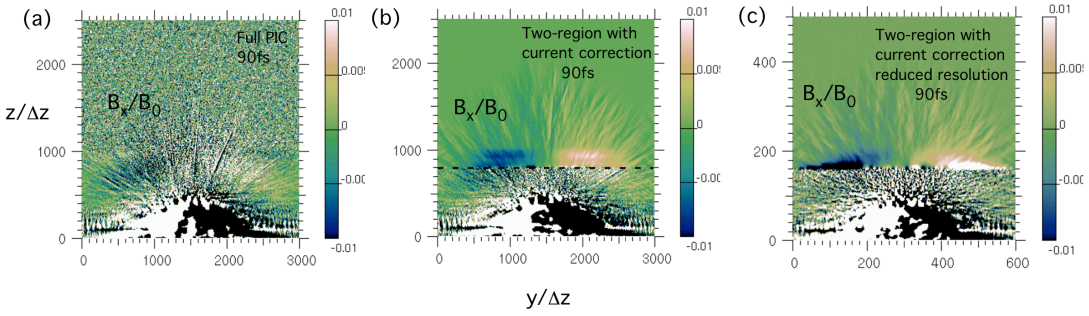

Figure 13: Two-dimensional PSC simulations extending the 1D simulations shown in Figs. 2, 7-9 to 2D: full PIC, two-region PIC-hybrid at full resolution (100 cpm), and two-region PIC-hybrid at reduced resolution (20 cpm) showing 2D contours of B_x at 90fs. $B_0 = E_0/c = 100$MG. (color online).

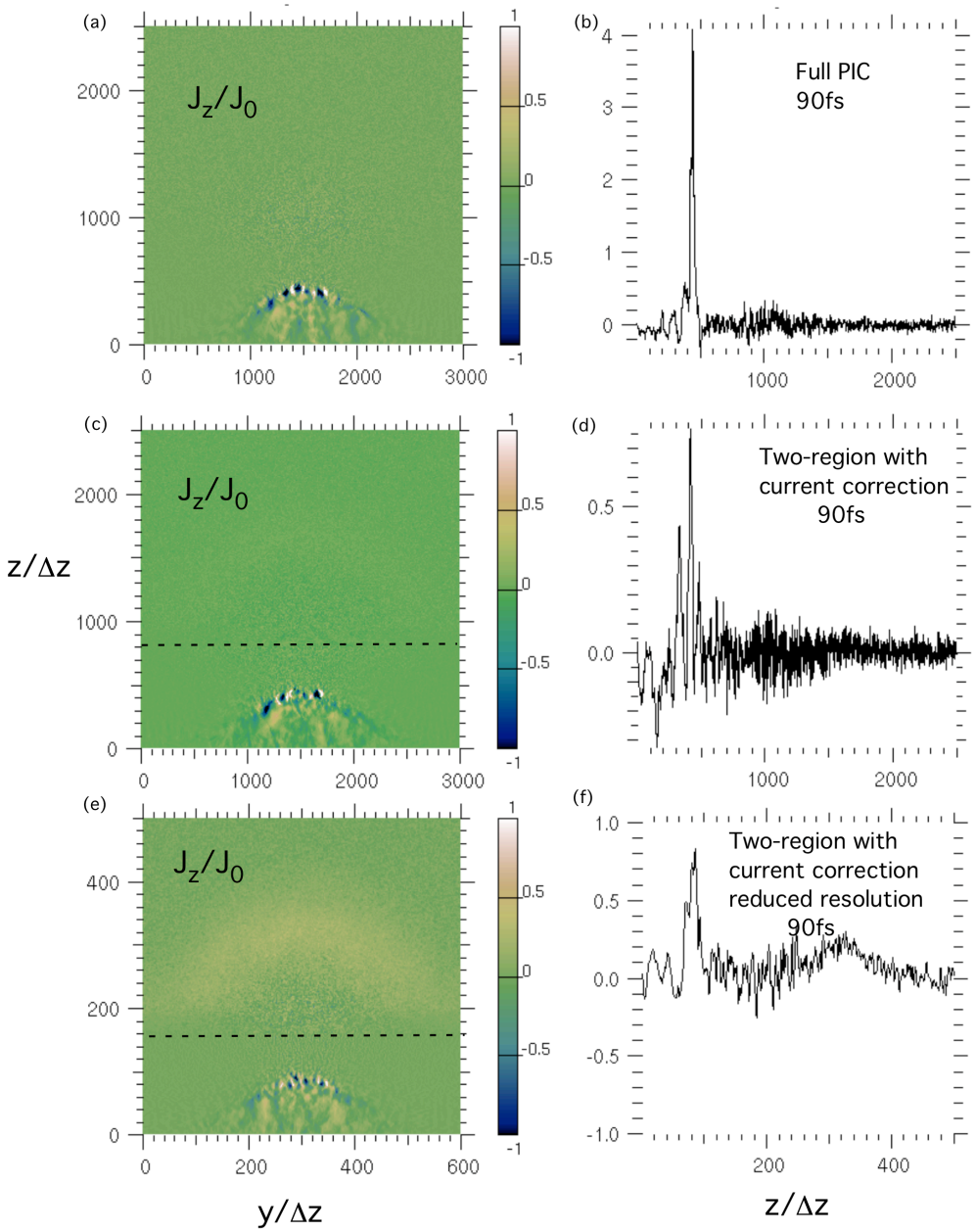

Figure 14: Two-dimensional PSC simulations extending the 1D simulations shown in Figs. 2, 7-9 to 2D: full PIC, two-region PIC-hybrid at full resolution (100 cpm), and two-region PIC-hybrid at reduced resolution (20 cpm) showing 2D contours and line-outs of the total current J_z vs. z in the midplane at 90fs. $J_0 = en_c c$. (color online)

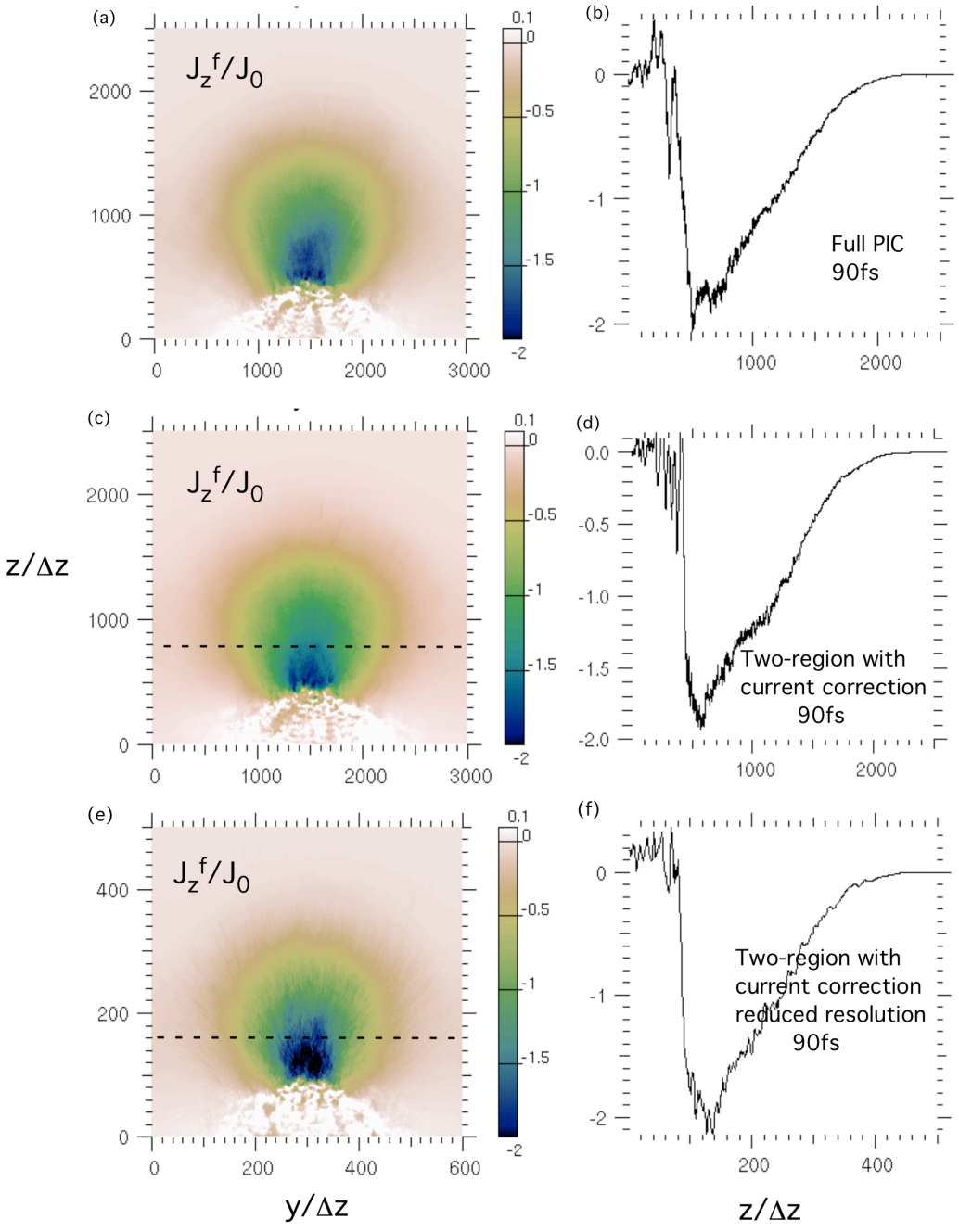

Figure 15: Two-dimensional PSC simulations extending the 1D simulations shown in Figs. 2, 7-9 to 2D: full PIC, two-region PIC-hybrid at full resolution (100 cpm), and two-region PIC-hybrid at reduced resolution (20 cpm) showing 2D contours and line-outs of the fast electron current J_z^f vs. z in the midplane at 90fs. $J_0 = en_c c$. (color online).